



# Time-averaged and transient pressure drop for flow boiling with saturated inlet conditions



Lucas E. O'Neill, Chirag R. Kharangate, Issam Mudawar\*

Boiling and Two-Phase Flow Laboratory (BTPFL), School of Mechanical Engineering, Purdue University, 585 Purdue Mall, West Lafayette, IN 47907, USA

## ARTICLE INFO

### Article history:

Received 20 May 2016

Received in revised form 10 July 2016

Accepted 11 July 2016

Available online 28 July 2016

### Keywords:

Flow boiling pressure drop

Pressure drop oscillations

Gravity effects

## ABSTRACT

This study explores flow boiling pressure drop of FC-72 in a rectangular channel subjected to single-side and double-sided heating for vertical upflow, vertical downflow, and horizontal flow with positive inlet quality. Analysis of temporal records of pressure transducer signals is used to assess the influences of orientation, mass velocity, inlet quality, heat flux, and single-sided versus double-sided heating on magnitude of pressure drop oscillations, while fast Fourier transforms of the same records are used to capture dominant frequencies of oscillations. Time-averaged pressure drop results are also presented, with trends focusing on the competing influences of body force and flow inertia, and particular attention paid to the impact of vapor content at the test section inlet and the rate of vapor generation within the test section on pressure drop. Several popular pressure drop correlations are evaluated against the present pressure drop database. Predictions are presented for subsets of the database corresponding to low and high ranges of inlet quality and mass velocity. The correlations are ranked based on mean absolute error, overall data trends, and data spread. While most show general success in capturing the data trends, they do so with varying degrees of accuracy.

© 2016 Elsevier Ltd. All rights reserved.

## 1. Introduction

### 1.1. Utilizing two-phase thermal management in next generation space missions

Two-phase thermal management systems offer vast improvements over their single-phase counterparts due to their utilization of both latent and sensible heat of the working fluid. With electronics across all industries trending towards smaller sizes and higher power consumption, the orders of magnitude enhancement in heat transfer offered by two-phase thermal management systems makes them ideal for cooling the next generation of high flux devices [1].

One area in which phase change systems show great promise is space, where their high heat transfer coefficients can play a significant role in reducing the size and weight of thermal management hardware. Because of this potential, space agencies worldwide are exploring the benefits and challenges associated with implementation of two-phase thermal management systems to support astronauts in both space vehicles and planetary bases. Current targets for implementation of phase change include Thermal Control

Systems (TCSs), which control the temperature and humidity of the operating environment, and Fission Power Systems (FPSs), which are projected to provide high power as well as low mass to power ratio [2–4].

Unlike thermal management of stationary Earth-based systems, use of two-phase cooling schemes for space applications entails the added complication of variable body force across missions. From hyper-gravity associated with launch, to microgravity encountered in orbit and interplanetary transit, to unique planetary gravitational environments associated with specific missions, thermal management systems designed to operate in space must be capable of performing in a broad range of gravitational accelerations. This greatly complicates the use of two-phase thermal management systems, where the orders of magnitude difference between phase densities causes body force (buoyancy) effects to affect flow behavior significantly.

Many previous studies have focused on different schemes for heat acquisition through boiling, including pool boiling thermosyphons [5,6], falling film [7–9], channel flow boiling [10], micro-channel boiling [11,12], jet impingement [13–15], and spray [16–18], as well as hybrid configurations [19] involving two or more of these schemes. While each possesses unique pros and cons, all suffer from a lack of understanding regarding the precise influence of body force on system heat transfer and pressure drop.

\* Corresponding author. Fax: +1 (765) 494 0539.

E-mail address: [mudawar@ecn.purdue.edu](mailto:mudawar@ecn.purdue.edu) (I. Mudawar).

URL: <https://engineering.purdue.edu/BTPFL> (I. Mudawar).



correlations. These correlations, commonly formulated in terms of relevant dimensionless groups, accurately recreate trends seen over very specific ranges of operating conditions, but often have trouble predicting pressure drop for physically relevant cases different from those used for correlation development. A recent review by Kim and Mudawar [20] attempted to alleviate these shortcomings by assembling a database composed of many different working fluids, test section geometries, and operating conditions, and using it to evaluate popular pressure drop correlations.

In contrast to the multitude of approaches taken to predicting system pressure drop, very little importance has been given to analyzing the transient nature of pressure (and thus pressure drop) in two-phase systems. The complex interplay between phases and the coupling of thermodynamic and hydrodynamic effects causes all two-phase systems to exhibit pressure fluctuations, which can vary significantly in magnitude depending on operating conditions and flow loop components. A classic review by Boure et al. [22] identified and labeled several instabilities common to flow boiling systems, such as pressure oscillations and density wave oscillations, but provided few tools for predicting their occurrence and impact on system performance.

Many recent reviews, such as those by Ruspini et al. [23], Kakac and Bon [24], and Tadrst [25], provide updated surveys of literature relating to phenomena first reported by Boure et al. [22], including overviews of analytic and numeric approaches adopted to modeling their behavior. However, it is evident that further work is necessary to develop a better fundamental understanding of instabilities and their impact on system performance.

### 1.3. Objectives of study

This study is part of a joint project between Purdue University Boiling and Two-Phase Flow Laboratory (PU-BTPFL) and NASA Glenn Research Center whose ultimate goal is to develop the Flow Boiling and Condensation Experiment (FBCE) for the International Space Station (ISS). The present study deals with the flow boiling portion of the project, and aims to use experimental results gathered in Earth's gravity to broaden understanding of the impact of body force on steady and transient system pressure.

Flow boiling experiments are performed in a rectangular channel with saturated inlet conditions at three orientations in Earth's gravity: vertical upflow, vertical downflow, and horizontal flow. The flow channel features two opposite heated walls that can be operated independently, allowing for tests in each orientation to be performed with single-sided or double-sided heating, with top and bottom wall heating being distinguished in horizontal flow. Analysis of experimental results will be undertaken with the aim of better understanding the parametric influences of mass velocity, inlet quality, and orientation (body force) on pressure drop.

Special attention will be paid to the transient behavior of pressure drop, something often overlooked when designing two-phase thermal management systems. As indicated above, the complex interplay between phases and the coupling of thermodynamic and hydrodynamic effects causes all two-phase systems to exhibit pressure fluctuations, and with few existing tools to model these effects, these fluctuations can represent a threat to successful operation of two-phase systems. Fast Fourier transforms of measured temporal records of pressure will be employed to identify dominant frequencies of oscillation as well as the amplitude of these oscillations across a broad range of operating conditions.

In an effort to complement previous studies at PU-BTPFL dealing mostly with prediction of critical heat flux [26–29], the present study will use experimental results to assess correlations for pressure drop commonly used in the literature, with the aim of determining how the various correlations perform for different flow orientations and ranges of operating conditions. Based on these

results, recommendations will be made on which correlations should be used for future work involving two-phase flow thermal management systems intended for operation in multiple gravitational environments.

## 2. Experimental methods

### 2.1. Flow boiling module

Part of FBCE slated for use on the ISS, the Flow Boiling Module (FBM) used in the present experiments is capable of acquiring accurate pressure drop and heat transfer measurements while simultaneously allowing for high-speed video imaging of the flow to be captured. Depicted in Fig. 1(a), the module is constructed from two transparent polycarbonate (Lexan) plates sandwiched between two aluminum support plates. Fig. 1(b) shows the middle Lexan plate is milled to create a rectangular 2.5-mm wide and 5-mm tall flow channel. The channel features an upstream development length of 327.9 mm, followed by a heated length of 114.6 mm, and an exit length of 60.9 mm.

Pressure measurements are made at five locations indicated in Fig. 1(a) using Honeywell STJE pressure transducers, including three within the development length, one upstream of the heated length, and one downstream of the heated length. Also indicated in Fig. 1(a) are locations of fluid temperature measurements corresponding to the channel's inlet and outlet. These measurements are made with type-E thermocouples inserted directly into the flow.

Copper slabs are inserted into grooves along the 2.5-mm sides of the heated length to serve as heated walls, with heat provided by six 4.5-mm wide, 16.4-mm long, and 188- $\Omega$  thick-film resistive heaters soldered to the backside of each copper slab as depicted in Fig. 1(c).

As depicted in Fig. 1(d), heated wall temperatures are measured by seven evenly spaced type-E thermocouples per wall. These thermocouples are designated as  $T_{wm,n}$ , where  $m$  represents the heated wall ( $H_a$  for heated wall  $a$  or  $H_b$  for heated wall  $b$ ), and  $n$  is the axial thermocouple location.

### 2.2. Two-phase flow loop

Desired inlet conditions for FBM are achieved using the flow loop shown schematically in Fig. 2(a). The working fluid, FC-72, is circulated in the loop using an Ismatech MCP-z magnetically-coupled gear pump located below the loop's reservoir. Exiting the pump, the fluid passes through a Shelco filter followed by a turbine flow meter, for accurate measurement of mass flow rate, before entering a set of two 1500-W Watlow preheaters to achieve a two-phase mixture at the inlet to the flow boiling module. Wall heat flux in the flow boiling module is controlled using the FBM heater control module depicted in Fig. 2(b). After passing through the flow boiling module, FC-72 is converted back to single-phase liquid by a tube-in-tube helical condenser using water supplied by a Lytron cooling system. The fluid then returns to the reservoir, which provides a reference pressure set point for the entire loop.

Data throughout the system are obtained with an NI SCXI-1000 data acquisition system controlled by a LabVIEW code. Pressure transducer data are sampled at 200 Hz, allowing high fidelity transient analysis of pressure signals.

Two-phase interfacial features are captured along the heated length of the flow boiling module using a high-speed camera. A fixed frame rate of 2000 frames per second (fps) and pixel resolution of 2040  $\times$  156 are used to capture images covering the entire 114.6-mm heated length for each test. Illumination is provided from the opposite side of the flow channel by four LEDs, with the

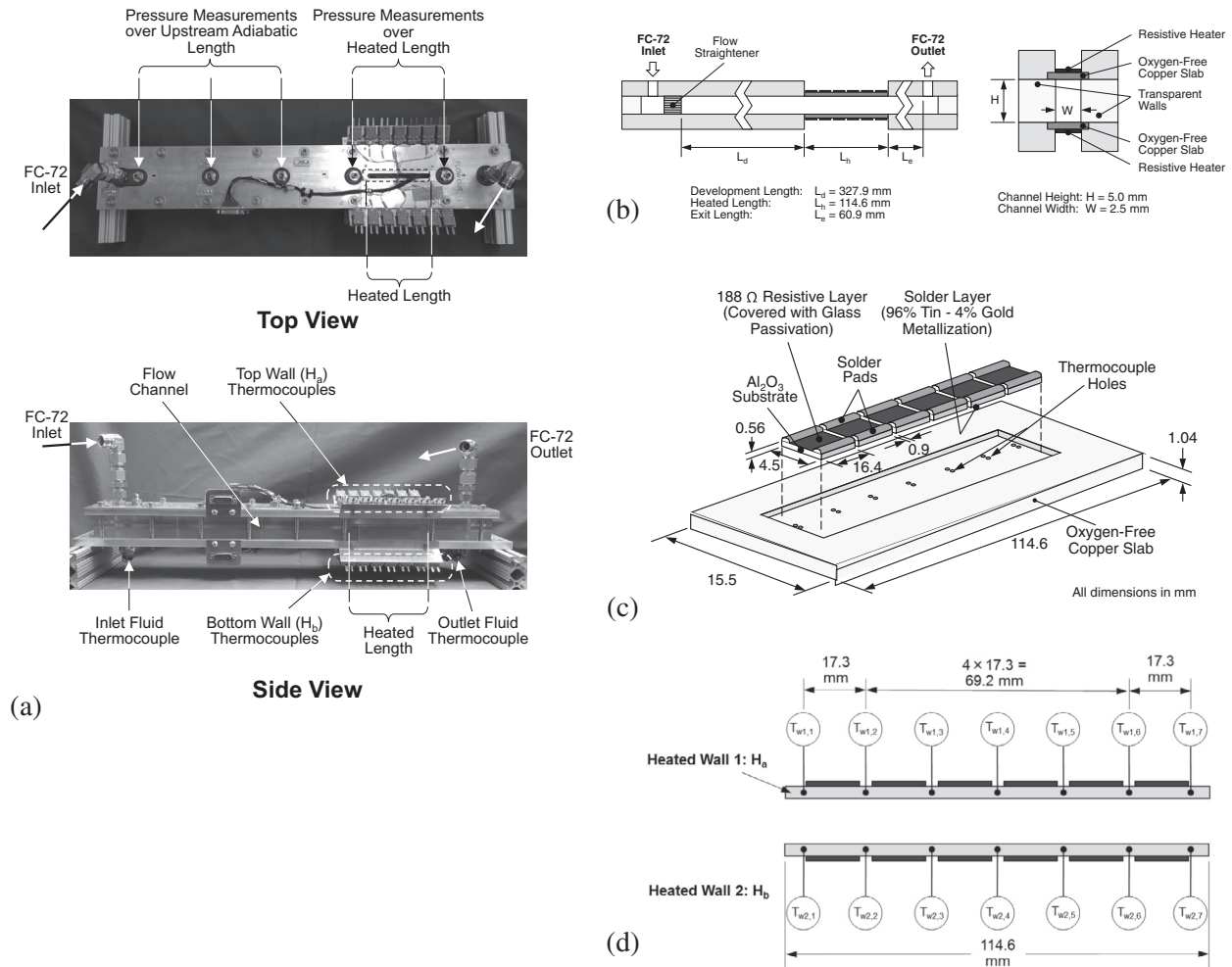


Fig. 1. (a) Top and side views of flow boiling module (FBM). (b) Flow channel schematic. (c) Construction of heated walls. (d) Heated wall thermocouples.

light passing through a light shaping diffuser (LSD) to enhance illumination uniformity.

### 2.3. Operating conditions, operating procedure and measurement uncertainty

Operating conditions spanning vertical upflow, vertical downflow, and horizontal flow orientations are: FC-72 inlet pressure of  $P_{in} = 109.7$ – $181.8$  kPa, inlet temperature of  $T_{in} = 54.2$ – $81.3$  °C, mass velocity of  $G = 183.5$ – $2030.3$  kg/m<sup>2</sup> s, and inlet thermodynamic equilibrium quality of  $x_{e,in} = 0.00$ – $0.69$ . Due to structural constraints of the flow boiling module, only the lowest mass velocities could be tested for the highest inlet qualities, and the highest mass velocities for the lowest inlet qualities. Table 1 provides the combinations and mass velocity and inlet quality achieved for all three flow orientations.

Tests are initiated by setting pump speed and pre-heater power to achieve the desired inlet conditions. After monitoring temperature and pressure signals in the LabVIEW code to confirm steady state has been reached, power to the specific heated wall(s) in the FBM is turned on, and heat flux is increased in small increments. After each increment, wall temperatures are monitored to determine if steady state is achieved, after which steady-state data are captured for 30–60 s. In this study, steady state is achieved when the wall and fluid temperatures cease to increase or decrease over a period of 15 s. Power is increased until critical heat flux

(CHF) is encountered, with the mass flow rate maintained by adjusting the pump's speed as necessary. To prevent the rapid temperature increase associated with CHF from damaging the flow boiling module, a secondary set of heated wall thermocouples are connected to power relays which disconnect power to the resistive heaters should wall temperature exceed 130 °C.

Type-E thermocouples with an accuracy of  $\pm 0.5$  °C are used to measure fluid and heated wall temperatures throughout the facility. Pressure measurements at the inlet of the upstream preheater and several locations along the flow boiling module are made with absolute pressure transducers with an accuracy of  $\pm 0.05\%$ , which corresponds to an accuracy for all pressure drop measurements of  $\pm 0.1\%$ . The turbine flow meter has an accuracy of  $\pm 0.1\%$ . The wall heat input is measured with an accuracy of  $\pm 0.5$  W.

## 3. Transient pressure results

### 3.1. Importance of characterizing amplitude and frequency of pressure oscillations

Commonly overlooked in studies focusing on two-phase flow, transient behavior of the system has the ability to greatly impact overall performance. In their seminal review, Boure et al. [22] discussed the tendency of two-phase flow systems to exhibit oscillations in pressure, mass velocity, and heat transfer performance, all with variable amplitude and frequency, depending on governing

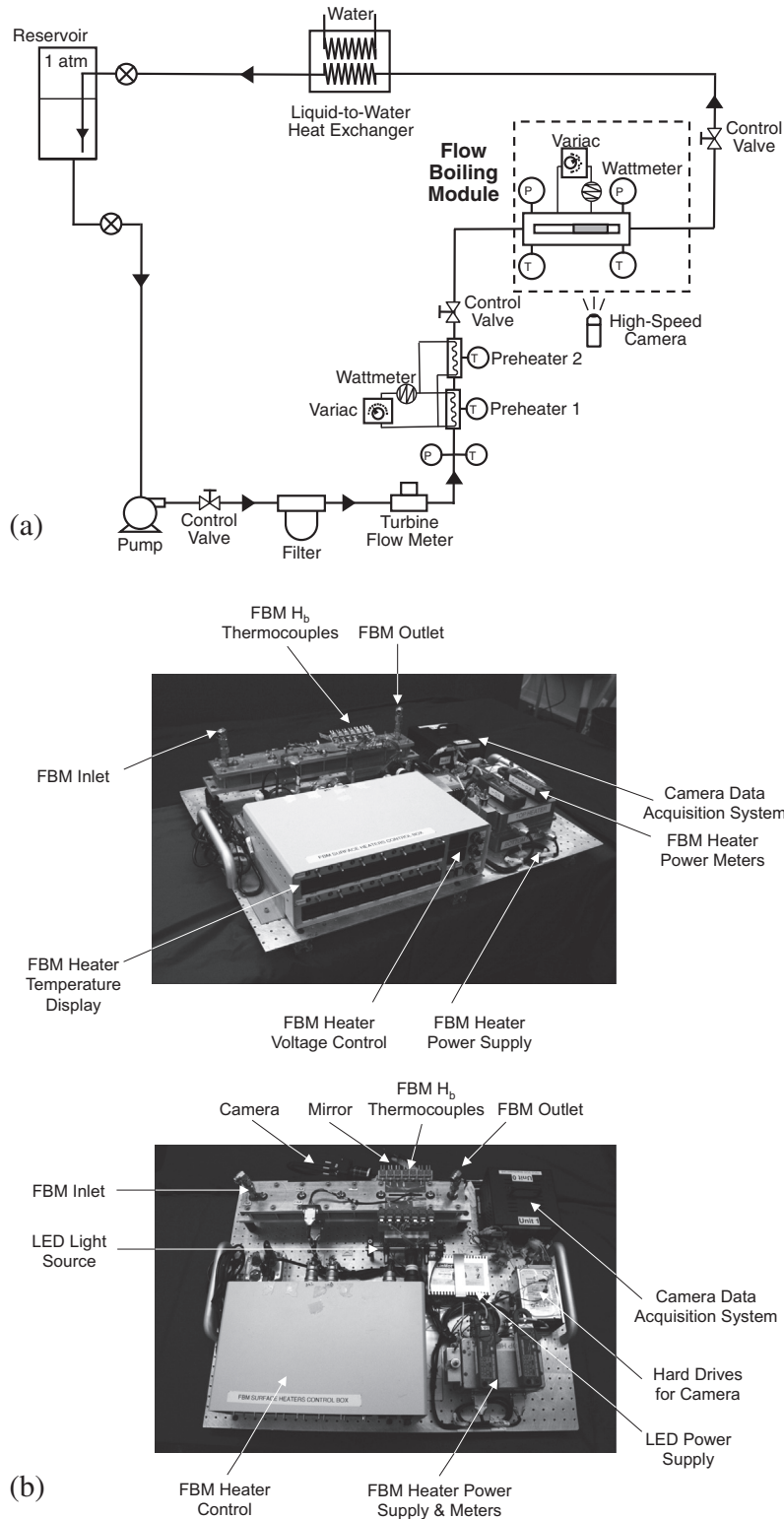


Fig. 2. (a) Flow loop diagram. (b) Photos of flow boiling module (FBM).

factors such as heat flux, mass velocity, and the fluid machinery in use.

While these fluctuations are often of secondary importance to “mean” (time-averaged) operating conditions, they have the capacity to compromise system safety in situations where nominal operations are near an important transitional point such as onset of

nucleate boiling (ONB), CHF, or two-phase choking. Additionally, use of control theory to provide constant operating conditions requires careful characterization of amplitude and frequency of oscillations. For these reasons, this section will analyze temporal records of pressure signals corresponding to a 30-s period after the system has become thermally steady. As mentioned in the

**Table 1**  
Test matrix for study.

Mass velocity, $G$ [kg/m <sup>2</sup> s]	Inlet quality, $x_{e,in}$								
	0.01	0.05	0.10	0.15	0.20	0.30	0.40	0.60	
~200	✓	✓	✓	✓	✓	✓	✓	✓	
~400	✓	✓	✓	✓	✓	✓	✓	✓	
~800	✓	✓	✓	✓	✓	✓	✓	NA	
~1200	✓	✓	✓	✓	✓	NA	NA	NA	
~1600	✓	✓	✓	NA	NA	NA	NA	NA	
~2000	✓	NA							

preceding section, a sampling rate of 200 Hz is used for all pressure measurements, allowing accurate transient analysis of frequencies up to 100 Hz (based on the Nyquist criterion).

### 3.2. Temporal records of heated section's inlet pressure, outlet pressure, and pressure drop

Fig. 3(a)–(c) show 30-s temporal records of pressure signals and accompanying amplitude–frequency plots for vertical upflow, vertical downflow, and horizontal flow, respectively, for identical inlet conditions of  $G = 800$  kg/m<sup>2</sup> s,  $x_{e,in} = 0$ , and  $q'' = 10.2$  W/cm<sup>2</sup>, and double-sided heating. Each figure includes records of inlet pressure,  $P_{in}$ , measured at the start of the heated length, outlet pressure,  $P_{out}$ , measured at the exit of the heated length, and two-phase pressure drop,  $\Delta P_{tp}$ , which is the difference of the two. It is important to note that for plots of amplitude versus frequency, a rise in amplitude as frequency approaches 0 (left edge of the plots) begins to represent time-averaged pressure drop, and as such does not offer information regarding transient behavior. For this reason, frequencies below 0.1 Hz (corresponding to oscillations with periods greater than 10 s) will not be included in subsequent analysis.

For vertical upflow, Fig. 3(a) shows pressure drop across the heated section ranges from 0 to 15 kPa, with a mean value of 7.1 kPa, indicating large fluctuations in operating conditions. Performing fast Fourier transforms of  $P_{in}$ ,  $P_{out}$  and  $\Delta P_{tp}$  signals yields a dominant frequency of oscillation (i.e., frequency corresponding to largest amplitude) of 2 Hz, with the peak exhibiting little sharpness, and relatively large amplitudes concentrated in a rather narrow frequency range between 0.5 and 6 Hz. This frequency range is consistent with those of *density wave oscillations*, which were attributed by Boure et al. [22] to “delay and feedback effects in relationship between flow rate, density, and pressure drop.” It is important to note that the plots in Fig. 3(a) provide no information on phase shift, as it is expected that a short period is required for conditions to propagate from inlet to outlet, which explains why the curves for inlet and outlet pressure do not perfectly align.

Amplitude–frequency plots for vertical upflow in Fig. 3(a) also reveal a secondary peak for  $P_{in}$  and  $\Delta P_{tp}$  around 20–25 Hz, something which is absent in the plot for  $P_{out}$ . It is suggested this secondary peak is the result of upstream pressure accounting for the added pressure resulting from “weight” of two-phase mixture along the heated section of the channel, which also changes due to temporal fluctuations of vapor void fraction.

In addition to the secondary peak, four very sharp peaks are seen at frequencies of exactly 20, 40, 60, and 80 Hz, ranging in magnitude from 0.1 to 0.2 kPa. These frequencies can be explained by the fact that the gear pump used in the two-phase loop operates at 60 Hz, meaning 80 Hz is an overtone, and 20 Hz and 40 Hz are subharmonics. This hypothesis is further substantiated by the fact that subharmonics commonly occur in frequency pairs whose sum equals that of the driving frequency [30].

Fig. 3(b) shows similar plots for vertical downflow. Here, however, pressure drop fluctuations range from 3 to 9 kPa, with a mean

value of 6.3 kPa, which are substantially smaller than the 0–15 kPa fluctuations encountered in vertical upflow. This is due to the weight of two-phase mixture decreasing pressure drop and amplitude of fluctuations in downflow. A Fast Fourier transform shows a dominant frequency of 0.7 Hz, which is smaller than the dominant frequency for vertical upflow. Fig. 3(b) also shows a secondary peak at 5–6 Hz, this time present for  $P_{out}$  and not  $P_{in}$ . Sharp peaks are again present at 20, 40, 60, and 80 Hz, indicating these sharp peaks are not influenced by body force.

Fig. 3(c) shows similar information for horizontal flow. Notice how pressure fluctuations for this orientation have a much smaller magnitude than those for vertical upflow and vertical downflow, presumably because of absence of axial body force effects. The pressure drop shows a mean value of 6.3 kPa, similar to that for vertical upflow and downflow, but a much reduced oscillation range of 5–8 kPa compared to 0–15 kPa for vertical upflow and 3–9 kPa of vertical downflow. Fig. 3(c) shows a dominant frequency for density wave oscillations around 0.3–0.4 Hz. The amplitude of oscillation is also lower for horizontal flow, with peak value of 0.4 kPa compared to 0.8 kPa for both vertical upflow and vertical downflow. Additionally, the secondary dominant frequency of 20–25 Hz for vertical upflow and 5–6 Hz for vertical downflow is absent for horizontal flow, indicating body force effects present for the vertical orientations are necessary for occurrence of the secondary frequency.

A comparison of  $P_{in}$ ,  $P_{out}$ , and  $\Delta P_{tp}$  signals for the different flow orientation shows all three signals exhibit fairly similar frequency content, especially around the dominant frequency range, and any behavior unique to  $P_{in}$  or  $P_{out}$  is also captured in the  $\Delta P_{tp}$  signal. For this reason, the transient pressure investigation will be focused hereafter on pressure drop.

### 3.3. Effects of heated wall configuration and mass velocity

Having determined that pressure drop between the inlet and outlet is sufficient to capture the relevant transient behavior, parametric evaluation of frequency content can be performed to determine the impact of heating configuration and mass velocity on transient aspects of pressure drop.

Fig. 4(a)–(d) show pressure drop amplitude–frequency plots for  $G \approx 200, 400, 800,$  and  $1600$  kg/m<sup>2</sup> s, respectively, corresponding to  $x_{e,in} = 0$  and  $q'' = 4.5$  W/cm<sup>2</sup>. Two key variables in these plots are flow orientation and heating configurations. As discussed earlier, three different flow orientations are examined: vertical upflow, vertical downflow, and horizontal flow. For vertical upflow and vertical downflow, two different heating configurations are considered, single-sided heating, where only one heating wall is energized, and double-sided heating, where both walls are energized simultaneously. For horizontal flow, relative position of the heated wall for single-sided heating is important due to transverse gravity effects across the channel. Therefore, three different configurations are considered for horizontal flow: single-sided top-wall heating, single-sided bottom-wall heating, and double-sided heating.

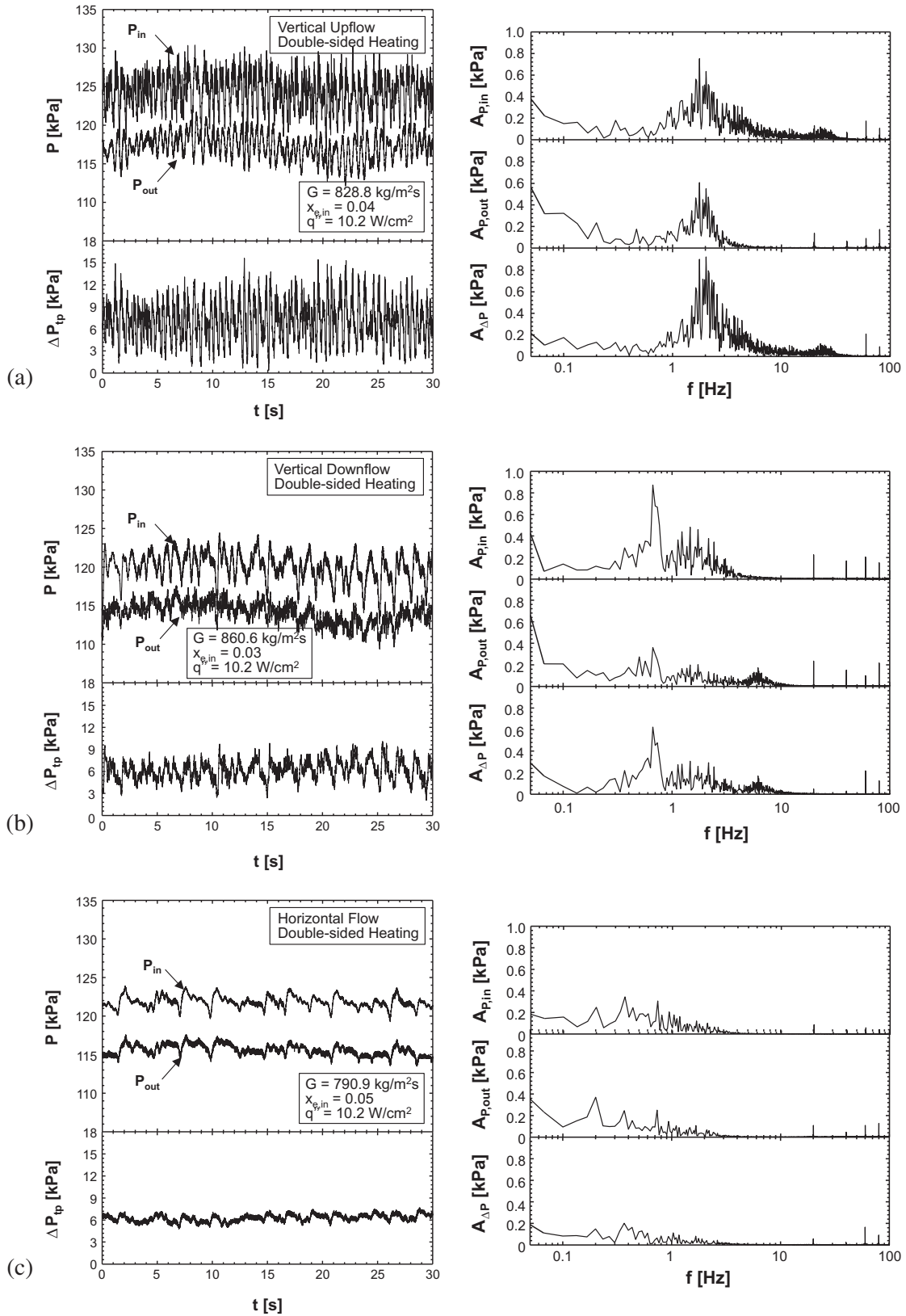


**Fig. 3.** Temporal records of heated section inlet pressure, outlet pressure, and pressure drop, and corresponding amplitude–frequency plots for double-sided heating in (a) vertical upflow, (b) vertical downflow, and (c) horizontal flow.

For the lowest mass velocity of  $G \approx 200 \text{ kg/m}^2 \text{ s}$ , Fig. 4(a) shows horizontal flow exhibits very minute pressure oscillations, with the highest amplitude associated with the 60-Hz pump frequency. Ver-

tical upflow again shows the highest amplitude oscillations around 0.5–6 Hz, compared to milder oscillations for vertical downflow around 1–10 Hz range. Yet, even for vertical upflow, pressure drop

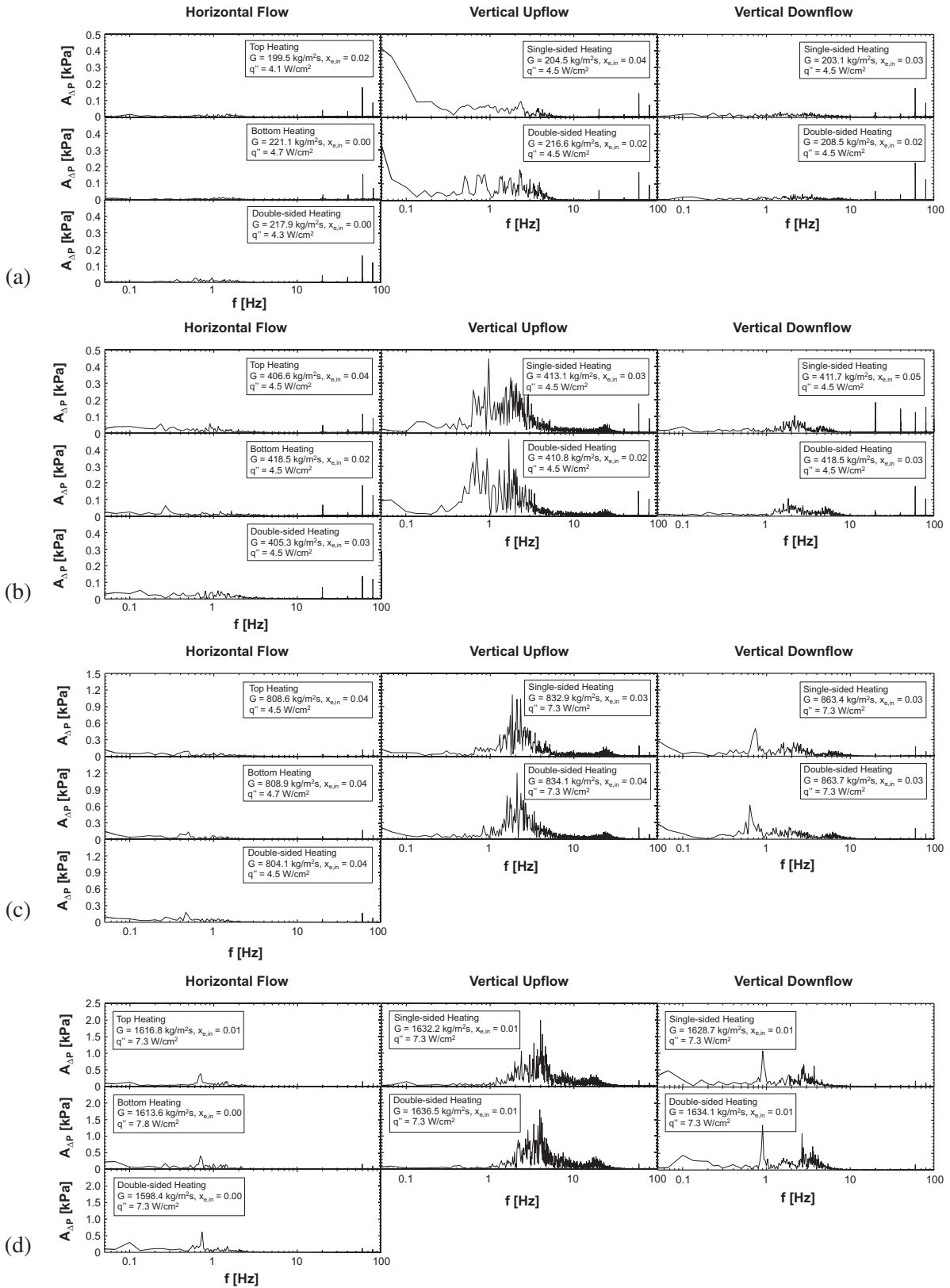


Fig. 4. Pressure drop amplitude–frequency plots for different orientations and (a)  $G = 199.5$ – $221.1$  kg/m<sup>2</sup> s, (b)  $G = 405.3$ – $418.5$  kg/m<sup>2</sup> s, (c)  $G = 804.1$ – $863.7$  kg/m<sup>2</sup> s, and (d)  $G = 1598.4$ – $1636.5$  kg/m<sup>2</sup> s.

oscillations are quite small for this low mass velocity range. The influence of heating configuration is captured only for vertical upflow, where double-sided heating is shown yielding slightly

higher peak amplitude compared to single-sided heating. The increased peak value is attributed to twice the amount of vapor being produced for double-sided compared to single-sided heating,

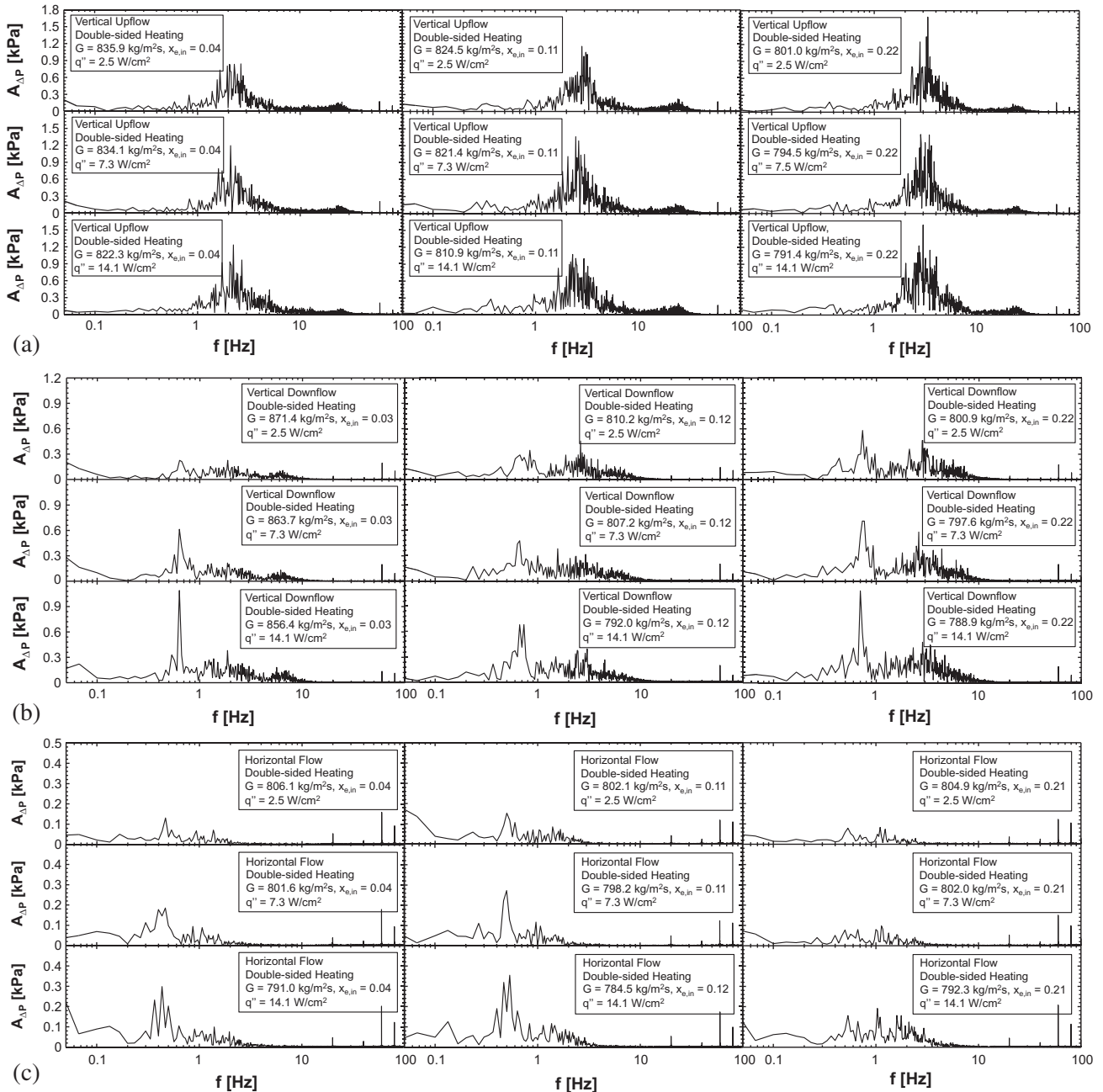


Fig. 5. Pressure drop amplitude–frequency plots for (a) vertical upflow, (b) vertical downflow, and (c) horizontal flow for double-sided heating and different inlet qualities and heat fluxes.

which is reflected in the influence of body force assisting vapor motion while hindering liquid flow. It should be noted that the influence of vapor generation on body force is especially pronounced at low mass velocities.

For a higher mass velocity of  $G \approx 400 \text{ kg/m}^2 \text{ s}$ , Fig. 4(b) shows oscillation amplitude remains near-zero for horizontal flow, but increases for both vertical upflow and vertical downflow. Once again, vertical upflow exhibits the highest amplitude, which is likely the result of density wave oscillations. Aside from dominant frequencies around 1–2 Hz, vertical upflow and vertical downflow show secondary amplitude bumps near 20–25 Hz and 5–10 Hz, respectively. Notice that, because of the reduced influence of vapor

generation on body force for this higher mass velocity, there are no significant differences in oscillation amplitude or frequency between single-sided and double-sided heating for the vertical orientations. It is also important to note that implicit in this result is the fact that exit quality, which is different for different heating configurations, does not directly affect system stability for the majority of cases.

Fig. 4(c) shows amplitude–frequency plots for a higher mass velocity of  $G \approx 800 \text{ kg/m}^2 \text{ s}$ . Here, again, vertical upflow exhibits pressure drop oscillations of significantly higher amplitude than vertical downflow or horizontal flow. However, vertical downflow exhibits peak amplitude around 0.6–0.7 Hz, much smaller than

that shown in Fig. 4(b). It is important to note the change in amplitude scale between Fig. 4(b) and (c), indicating the amplitude of pressure drop oscillations increases with increasing  $G$ .

For the highest mass velocity of  $G \approx 1600 \text{ kg/m}^2 \text{ s}$ , Fig. 4(d) again shows vertical upflow exhibiting the largest amplitude oscillations. Horizontal flow now also exhibits a clearly identifiable peak around 0.7–0.8 Hz, consistent with density wave oscillations, although its amplitude remains much smaller than those of vertical upflow and vertical downflow. Here, too, it is important to note the change in amplitude scale between Fig. 4(c) and (d), indicating oscillations continue to grow in amplitude with increasing  $G$ .

Comparing Fig. 4(a)–(d) reveals important trends concerning the influence of flow orientation and mass velocity on pressure drop oscillation amplitude and frequency. First, notice that the emergence of a pronounced peak amplitude occurs first for vertical upflow at  $G \approx 400 \text{ kg/m}^2 \text{ s}$ , followed by vertical downflow at  $G \approx 800 \text{ kg/m}^2 \text{ s}$ , and eventually by horizontal flow at  $G \approx 1600 \text{ kg/m}^2 \text{ s}$ . Additionally, both peak amplitude and dominant frequency increase monotonically with increasing mass velocity for all orientations. This indicates the mechanism behind peak amplitude and dominant frequency is tied to both body force and flow inertia.

Excepting vertical upflow at the lowest mass velocity of  $G \approx 200 \text{ kg/m}^2 \text{ s}$ , no appreciable differences are detected between single-sided and double-sided heating configurations. Therefore, all subsequent transient analysis will be focused on double-sided heating. The drastic differences in amplitude between orientations is likely due to gravity's role acting against fluid motion, and therefore both increasing pressure drop and intensifying oscillations, in vertical upflow, while acting against fluid motion in vertical downflow. Being devoid of gravity effects along the flow direction, horizontal flow exhibits almost no oscillations for low mass velocities.

### 3.4. Effects of heat flux and inlet quality

Fig. 5(a)–(c) show amplitude–frequency plots for pressure drop in vertical upflow, vertical downflow, and horizontal flow, respectively, for  $G \approx 800 \text{ kg/m}^2 \text{ s}$  and double-sided heating. Results are shown for heat fluxes of  $q'' = 2.5, 7.3, \text{ and } 14.1 \text{ W/cm}^2$  and inlet qualities of  $x_{e,in} \approx 0, 0.10, \text{ and } 0.20$ . It is important to note that the maximum y-axis scale decreases from 1.8 kPa in Fig. 5 (a), to 1.2 kPa in Fig. 5(b), all the way to 0.5 kPa in Fig. 5(c), further reinforcing the trends of decreasing amplitude of pressure drop oscillation from vertical upflow to vertical downflow to horizontal flow captured earlier in Fig. 4(a)–(d).

Fig. 5(a) shows, for vertical upflow, that the amplitude of pressure drop oscillations increases as heat flux is increased towards CHF. This makes intuitive sense, as more intense vapor generation creates greater axial fluctuations in frictional, accelerational and gravitational pressure drop. For the same reason, the amplitude increases with increasing inlet quality, with the case corresponding to maximum heat flux of  $q'' = 14.1 \text{ W/cm}^2$  and maximum inlet quality of  $x_{e,in} = 0.22$  exhibiting the strongest pressure drop oscillations across the range of frequencies investigated.

For vertical downflow, Fig. 5(b) shows that the amplitude of oscillation again increases with increasing heat flux. Less obvious is the trend relative to inlet quality, with peak amplitude decreasing as  $x_{e,in}$  is increased from 0 to 0.10 before increasing again between 0.10 and 0.20. Nonetheless, secondary oscillations in the range of 1–10 Hz, which are of lower magnitude than the peak corresponding to 0.6–0.7 Hz, show consistent increases in amplitude as  $x_{e,in}$  is increased from  $x_{e,in} \approx 0$  to 0.20. This may point to differences in mechanisms behind pressure oscillations in the two frequency ranges.

For horizontal flow, Fig. 5(c) further reinforces the trend of amplitude increasing with heat flux. The amplitude remains

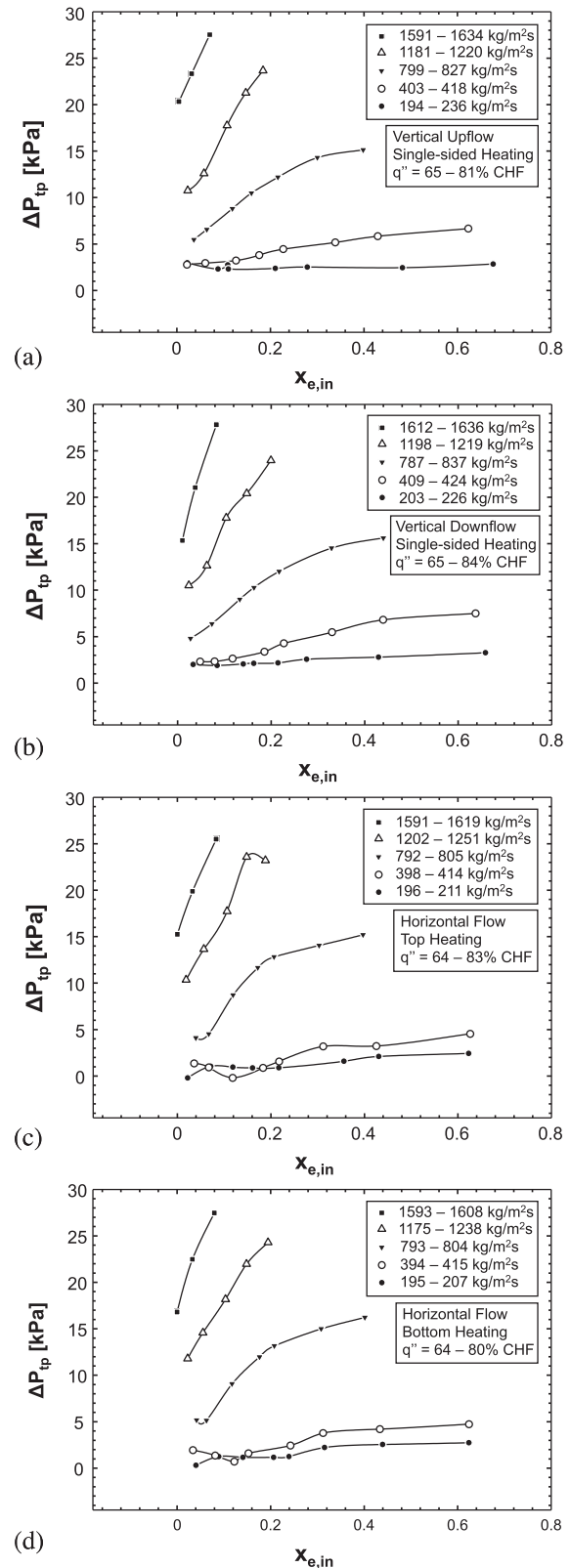


Fig. 6. Pressure drop versus inlet quality for single-sided heating in (a) vertical upflow, (b) vertical downflow, (c) horizontal flow with top heating, and (d) horizontal flow with bottom heating.

mostly constant for  $x_{e,in} \approx 0$ –0.10 before decreasing for  $x_{e,in} \approx 0.10$ –0.20, indicating that increased vapor content in horizontal flow acts as a dampening agent for pressure oscillations. This effect can be attributed to the secondary role of body force

acting to stratify horizontal flow with high vapor content, accumulating vapor along the top wall and liquid along the bottom, a phenomenon not present in vertical flow orientations.

#### 4. Time-averaged pressure drop

##### 4.1. Components of total two-phase pressure drop

Pressure drop in two phase flows,  $\Delta P_{tp}$ , is comprised of three components and governed by the relation

$$\Delta P_{tp} = \Delta P_F + \Delta P_G + \Delta P_A, \quad (1)$$

where  $\Delta P_F$ ,  $\Delta P_G$ , and  $\Delta P_A$  are the pressure drop components associated with friction, gravity, and flow acceleration, respectively. The competing influences of these three components complicate predictions of total pressure drop, and parametric assessment of the influences of mass velocity, body force, and flow quality is necessary to further understand the interplay between components.

The preceding section examined transient fluctuations of pressure drop in detail for all orientations and a broad range of operating conditions. Much more important to conventional system design, however, is the magnitude of total “mean” (time-averaged) pressure drop. This section will therefore focus on trends in total mean pressure drop data by examining results time-averaged over a 20-s period after the system has reached steady state.

##### 4.2. Effects of inlet quality

Fig. 6(a)–(d) show, for single-sided heating, variations of  $\Delta P_{tp}$  across the heated section of the channel with inlet quality for different mass velocities in vertical upflow, vertical downflow, horizontal flow with top heating, and horizontal flow with bottom heating, respectively.

Fig. 6(a) shows that pressure drop for vertical upflow is relatively flat for the lowest mass velocity of  $G \approx 200 \text{ kg/m}^2 \text{ s}$ , but exhibits an increasingly stronger relationship with  $x_{e,in}$  as mass velocity

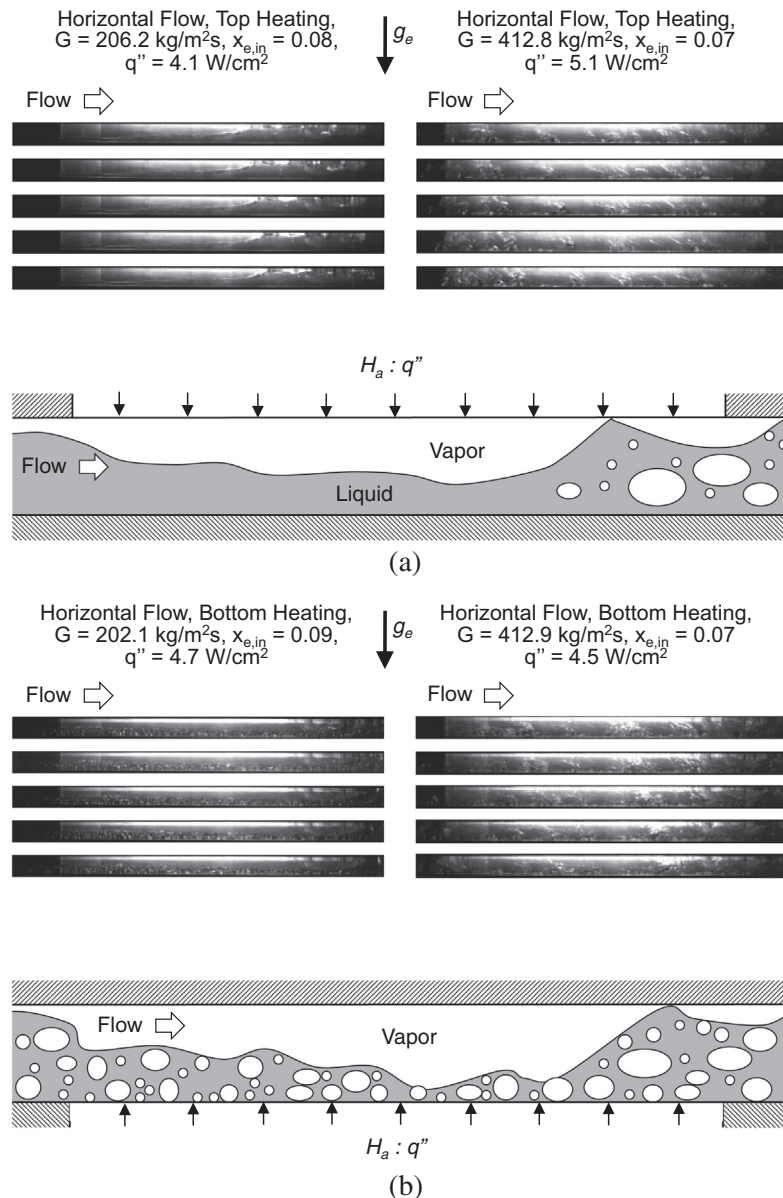


Fig. 7. Vapor accumulation along top wall for horizontal flow with (a) top heating and (b) bottom heating.

is increased, with the highest mass velocity of  $G \approx 1600 \text{ kg/m}^2 \text{ s}$  exhibiting a 3–5 kPa increase in pressure drop as  $x_{e,in}$  is increased from 0–0.05 to 0.05–0.10. The increase in pressure drop appears to slow with further increases in  $x_{e,in}$ , as seen clearly for  $G \approx 800 \text{ kg/m}^2 \text{ s}$ . This trend can be explained by a large increase in vapor void fraction towards unity and the flow approaching pure vapor flow by volume, for which a constant pressure drop is expected.

Fairly similar behavior is seen in Fig. 6(b) corresponding to vertical downflow. For horizontal flow with top heating, Fig. 6(c) shows  $\Delta P_{tp}$  values lower than those for vertical upflow for low inlet qualities corresponding to relatively high liquid content. This can be explained by the absence of a gravitational component of pressure drop for horizontal orientations. However, this effect becomes less pronounced as  $x_{e,in}$  is increased further, and pressure drop results for the highest  $x_{e,in}$  cases are fairly similar to those for vertical upflow and vertical downflow. For horizontal flow with bottom heating, Fig. 6(d) shows overall trends similar to those for top heating.

Notice that, unlike the two vertical orientations, horizontal flows with both top heating and bottom heating show near-zero pressure drop for low qualities and the two lowest mass velocities. These conditions are associated with low flow inertia, and weak ability to purge vapor accumulated along the top wall. Because stratification effects across the channel are strongest for horizontal flow with low  $x_{e,in}$  and low  $G$ , vapor is accumulated along the top wall for both top and bottom heating. The vapor accumulation along the top portion of the channel exposes a substantial portion of the channel's perimeter to low-viscosity vapor, reducing the frictional component of pressure drop. On the other hand, both vertical upflow and vertical downflow tend to push liquid towards the wall, surrounding a central vapor core, exposing most of the channel's perimeter to high-viscosity liquid. This increases friction for the two vertical orientations, resulting in  $\Delta P_{tp}$  values at low  $x_{e,in}$  and low  $G$  far greater than those for the two horizontal flows.

These low  $x_{e,in}$  and low  $G$  phenomena are further examined in Fig. 7(a) and (b), for horizontal flow with top heating and bottom heating, respectively, by comparing interfacial behavior for  $G = 202.1\text{--}206.2 \text{ kg/m}^2 \text{ s}$ ,  $x_{e,in} = 0.08\text{--}0.09$ , and  $q'' = 4.1\text{--}4.7 \text{ W/cm}^2$  with that for  $G = 412.8\text{--}412.9 \text{ kg/m}^2 \text{ s}$ ,  $x_{e,in} = 0.07$ , and  $q'' = 4.5\text{--}5.1 \text{ W/cm}^2$ . Shown for each case is a series of images of the flow, with individual images separated by 2.5 ms. For top heating at  $G = 206.2 \text{ kg/m}^2 \text{ s}$ , Fig. 7(a) clearly shows the top wall exposed mostly to vapor, with only small portions in contact with liquid. It is these intermittent liquid contact regions that are responsible for most of the top-wall cooling for this nearly-stratified horizontal flow. For top heating at the higher mass velocity of  $G = 412.8 \text{ kg/m}^2 \text{ s}$ , Fig. 7(a) shows increased flow inertia resisting stratification effects and fostering vapor entrainment along the flow direction, which greatly increases top wall exposure to liquid.

Fig. 7(b) shows trends for horizontal flow with bottom heating. For  $G = 202.1 \text{ kg/m}^2 \text{ s}$ , vigorous nucleate boiling is seen taking place along the bottom wall. However, stratification causes the vapor to accumulate along the top wall, similar to the top heating behavior captured in Fig. 7(a). Here, again, a large portion of the top wall is exposed to low-viscosity vapor, which decreases the frictional pressure drop when compared to flow regimes exhibiting full circumferential liquid exposure. For bottom heating at the higher mass velocity of  $G = 412.9 \text{ kg/m}^2 \text{ s}$ , Fig. 7(b) shows increased inertia causing the vapor generated along the bottom wall to be entrained along the flow direction, and increasing top wall exposure to liquid, resulting in greater frictional pressure drop. Further increases in mass velocity cause horizontal flow cases to exhibit fully annular flow, similar to that encountered in vertical upflow and downflow orientations for all test conditions.

Fig. 8(a)–(c) show, for double-sided heating,  $\Delta P_{tp}$  versus  $x_{e,in}$  for vertical upflow, vertical downflow, and horizontal flow, respectively. Fig. 8(a) and (b) show pressure drop trends for vertical upflow and vertical downflow, respectively, similar to their single-sided counterparts shown earlier in Fig. 6(a) and (b). However, both the magnitude of  $\Delta P_{tp}$  and the rate at which  $\Delta P_{tp}$  increases with  $x_{e,in}$  are greater for double-sided heating. This is the outcome of doubling the amount of heat added to the flow per unit length, effectively doubling the acceleration component of pressure drop.

Again, pressure drop for double-sided heating with  $x_{e,in} \approx 0$  is consistently lower for vertical downflow compared to vertical upflow due to body force increasing pressure drop for vertical

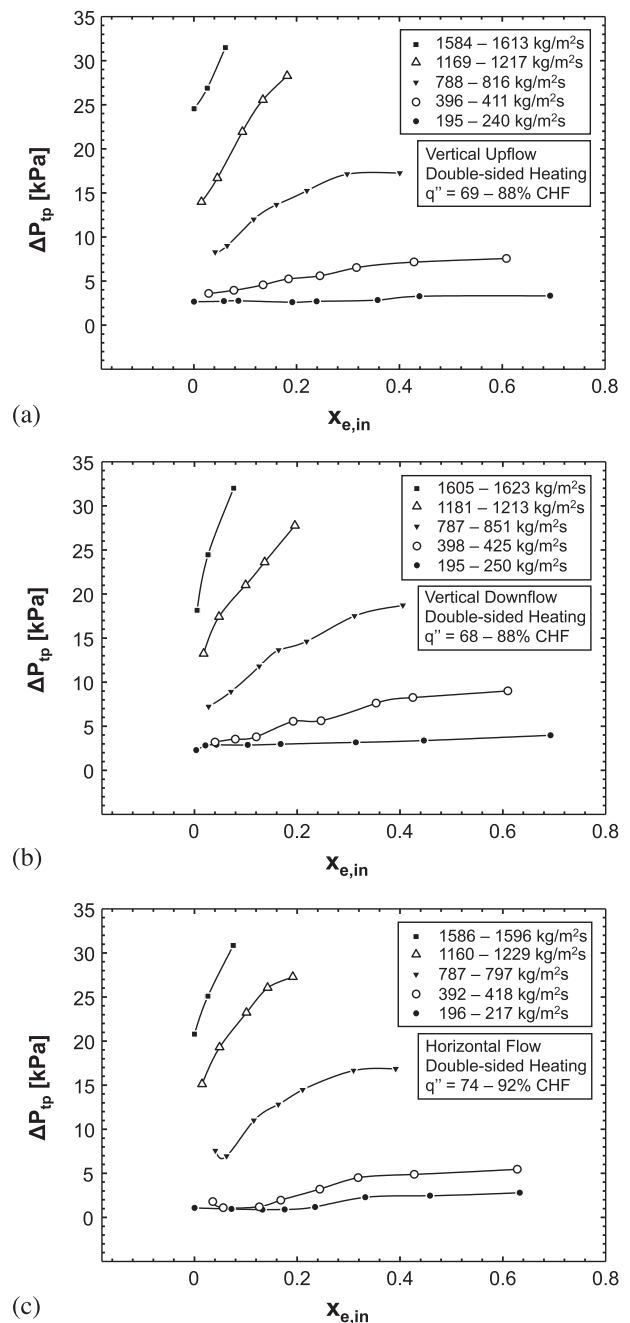
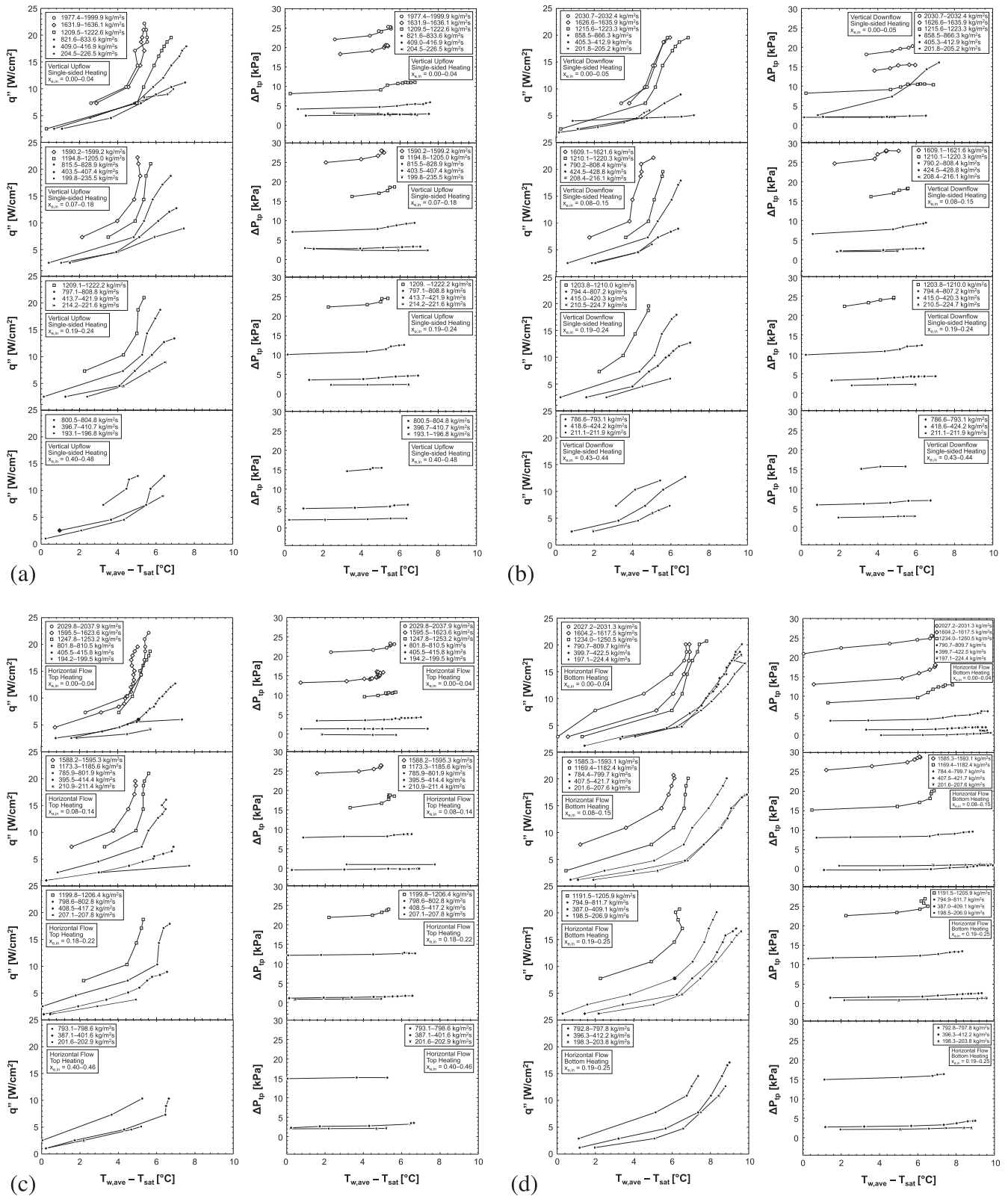


Fig. 8. Pressure drop versus inlet quality for double-sided heating in (a) vertical upflow, (b) vertical downflow, and (c) horizontal flow.



**Fig. 9.** Variations of wall heat flux and pressure drop across heated section of flow channel with average wall temperature minus saturation temperature for single-sided heating in (a) vertical upflow, (b) vertical downflow, (c) horizontal flow with top heating, and (d) horizontal flow with bottom heating.

upflow while decreasing pressure drop for vertical downflow. This effect diminishes with increasing  $x_{e,in}$  faster than with single-sided heating as double-sided heating further increases vapor void fraction and therefore decreases the contribution of gravitational pressure drop.

For horizontal flow with double-sided heating, Fig. 8(c) shows  $\Delta P_{tp}$  trends similar to those for single-sided heating and shown in Fig. 6(c) and (d). Here again, an increase in acceleration pressure drop due to increased heat addition increases both  $\Delta P_{tp}$  and the rate at which  $\Delta P_{tp}$  increases with  $x_{e,in}$ . However, the vapor

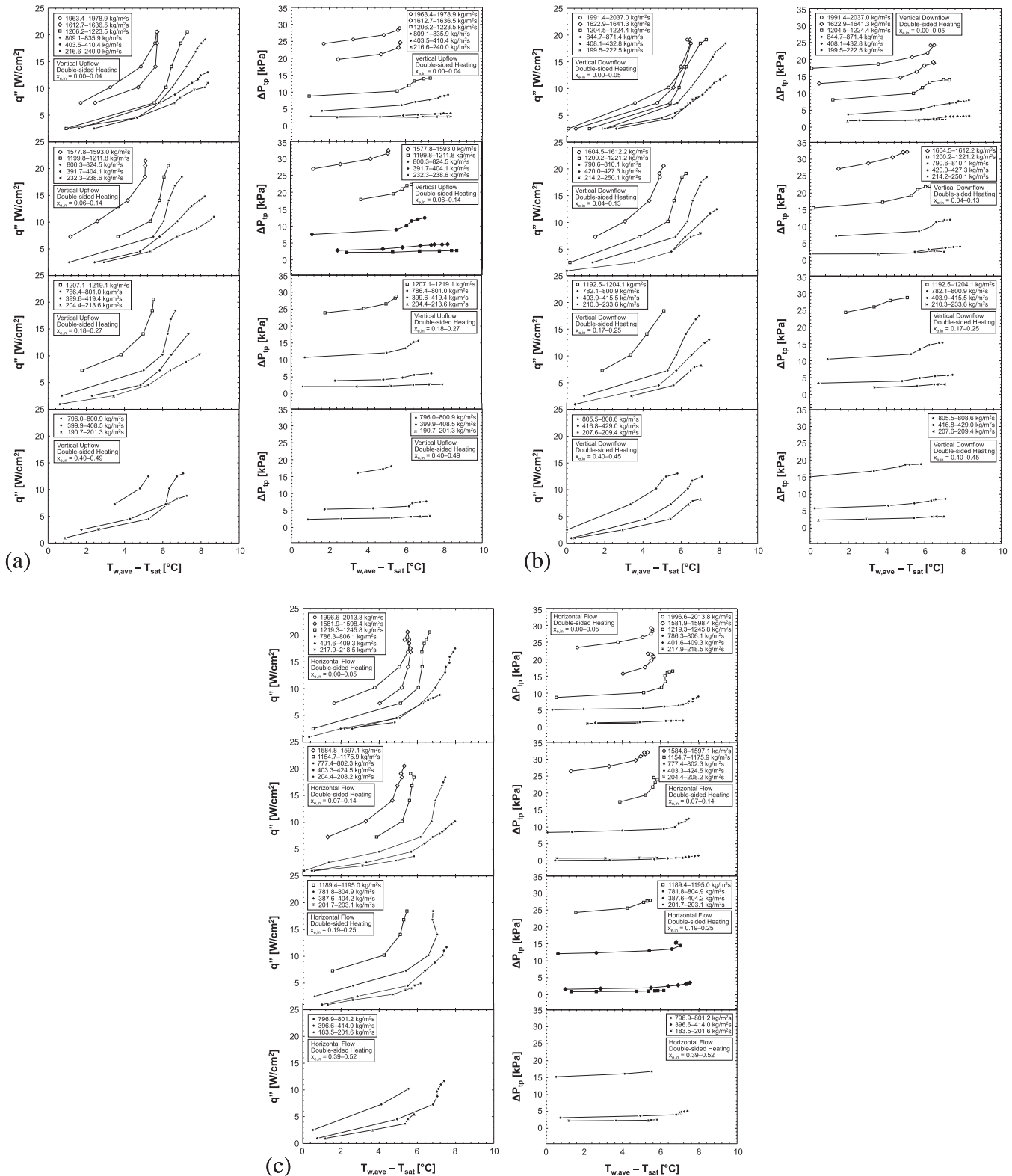


Fig. 10. Variations of wall heat flux and pressure drop across heated section of flow channel with average wall temperature minus saturation temperature for double-sided heating in (a) vertical upflow, (b) vertical downflow, and (c) horizontal flow.

stratification effect captured earlier in Fig. 7(a) and (b) is less noticeable. This is due to the formation of vapor along both walls driving the flow pattern to something closer to churn flow compared to the stratified flow seen with single-sided heating.

For vertical upflow with single-sided heating, a plateauing in the variation of  $\Delta P_{tp}$  with  $x_{e,in}$  was shown in Fig. 6(a), especially for  $G \approx 400$  and  $800 \text{ kg/m}^2 \text{ s}$ . For double-sided heating, Fig. 8(a) shows a much more noticeable plateauing effect, with the high

$x_{e,in}$  ranges for  $G \approx 200, 400,$  and  $800 \text{ kg/m}^2 \text{ s}$  exhibiting almost no change in  $\Delta P_{tp}$ . This trend can be attributed to increased heat addition yielding vapor void fractions approaching unity earlier than with single-sided heating.

#### 4.3. Effects of heat flux

Thus far, much of the discussion of time-averaged pressure drop has been focused on the influence of vapor content at the inlet to the heated section of the channel, which is reflected in the magnitude of inlet quality. Further vapor production is achieved along the heated section due to heat addition, and this effect is manifest to different degrees in all components of  $\Delta P_{tp}$ .

Fig. 9(a)–(d) show plots of heat flux versus average wall superheat,  $T_{w,ave} - T_{sat,in}$ , side-by-side with plots of total pressure drop versus average wall superheat, for single-sided heating in vertical upflow, vertical downflow, horizontal flow with top heating, and horizontal flow with bottom heating, respectively. This side-by-side layout allows detailed examination of how pressure drop increases as heat flux is increased towards CHF. For all orientations, inlet qualities of  $x_{e,in} \approx 0, 0.10, 0.20,$  and  $0.40$  are targeted, and the full range of mass velocities achieved for each quality is investigated.

For vertical upflow, Fig. 9(a) shows a noticeable increase in  $\Delta P_{tp}$  with increasing heat flux for all inlet qualities. This figure shows an interesting behavior for the mid-range mass velocities of  $G \approx 800$  and  $1200 \text{ kg/m}^2 \text{ s}$  near  $6^\circ\text{C}$  wall superheat, where  $\Delta P_{tp}$  curves become non-linear, exhibiting a steep increase for one to two data points before flattening out again just prior to CHF. This steep increase is not readily apparent for the two lowest mass velocities, and the plateauing effect is not discernible for the two highest mass velocities. Fig. 9(a) also shows the rate of increase in  $\Delta P_{tp}$  with heat flux increases with increasing mass velocity. This can be explained by the dependence of frictional and accelerational components of pressure drop on  $G^2$ . The boiling curves themselves all exhibit a sharp increase in slope shortly before this point. This slope change is attributed to commencement of nucleate boiling along the heated wall.

For the case of vertical downflow with single-sided heating, Fig. 9(b) displays the same large increase in  $\Delta P_{tp}$  midway along the boiling curve before plateauing at higher heat fluxes. It should be noted that this is different from the plateauing effect described in the preceding section, which requires high qualities to manifest, while the plateauing in Fig. 9(b) occurs at low qualities.

Horizontal flow with top heating, Fig. 9(c), exhibits much milder increases in  $\Delta P_{tp}$  with increasing heat flux compared to those for vertical upflow and vertical downflow, with only the two highest mass velocities exhibiting behavior resembling those in Fig. 9(a) and (b). The milder increase in  $\Delta P_{tp}$  at low mass velocities is likely the result of the vapor stratification and coverage of the top wall as depicted in Fig. 7(a). For horizontal flow with bottom heating, Fig. 9(d) reinforces this trend for low mass velocities, but reverts to behavior closer to that for vertical upflow and vertical downflow at lower mass velocities than to horizontal flow with top heating.

Similar results for double-sided heating in vertical upflow, vertical downflow, and horizontal flow are shown in Fig. 10(a)–(c), respectively. The trends here are very close to those for single-sided heating, the key difference being that vapor stratification effects are no longer critical for horizontal flow, mimicking the conclusion drawn from comparing Fig. 6(c) and (d) with Fig. 8(c).

Another important takeaway from Fig. 10(a)–(c) is the manifestation of an exponential pressure drop increase before plateauing at lower mass velocities, especially for vertical upflow and vertical downflow. As indicated earlier, amplitude of pressure drop is also greater for double-sided heating than single-sided, with differ-

ences of 5 kPa or larger for many sets of operating conditions. This indicates this phenomenon is sensitive not only to heat flux but to total heat input. However, as there is no appreciable change in the exponential increase with increasing inlet quality, the idea that this phenomenon is associated with changes in hydrodynamic development due to increased vapor addition within the heated length and not simply flow acceleration is further reinforced.

## 5. Assessment of predictive capabilities

### 5.1. Pressure drop database

The discussion of competing influences of mass velocity, inlet quality, channel orientation, and wall heating configuration in the preceding sections provides valuable qualitative insight into pressure drop trends. However, quantitative assessment of the same parameters requires comparison of the present pressure drop data against available predictive tools. Empirical and semi-empirical correlations have long served as standard tools by those designing two-phase thermal management systems. This section will assess the predictive accuracy of popular correlations by comparing predicted values against a database consisting of 829 time-averaged pressure drop measurements obtained in the present study. This database is a subset of the measured pressure drops, and corresponds to heat fluxes between 35% and 90% of CHF, chosen to represent nominal operating conditions for many two-phase thermal management systems.

The primary measure for accuracy of individual correlations used here is Mean Absolute Error (MAE), which is defined as

$$MAE = \frac{1}{N} \sum \frac{|\Delta P_{tp,pred} - \Delta P_{tp,exp}|}{\Delta P_{tp,exp}} \times 100\%. \quad (2)$$

Additionally, as correlation performance may be skewed for particular subsets of data while performing well for others, quantities  $\theta$  and  $\zeta$  are presented to indicate the percentage of predictions falling within 30% and 50% of experimental values, respectively.

### 5.2. Pressure drop models and correlations

As defined in Eq. (1), pressure drop for two-phase flow is comprised of frictional, gravitational, and acceleration components. Table 2 presents both models and correlations for two-phase frictional pressure gradient,  $-(dP/dz)_F$ , that are examined in this study. They include two main categories: those based on the Homogeneous Equilibrium Model (HEM), and others that are empirical in nature. Components due to gravity and flow acceleration are according to

$$-\left(\frac{dP}{dz}\right)_G = [\alpha\rho_g + (1-\alpha)\rho_f]g \sin\psi \quad (3)$$

and

$$-\left(\frac{dP}{dz}\right)_A = G^2 \frac{d}{dz} \left[ \frac{v_g x^2}{\alpha} + \frac{v_f (1-x)^2}{(1-\alpha)} \right] \quad (4)$$

respectively, where  $\alpha$  is local void fraction and  $\psi$  is the angle of orientation of the flow channel relative to gravity. The void fraction is calculated using Zivi's correlation [47], defined as

$$\alpha = \left[ 1 + \left( \frac{1-x}{x} \right) \left( \frac{\rho_g}{\rho_f} \right)^{2/3} \right]^{-1}. \quad (5)$$

Total pressure drop is calculated by dividing the channel length into 645 segments and marching forward, using local quality at each

**Table 2**  
Pressure drop correlations for evaluation.

Author(s)	Equation(s)	Remarks
McAdams et al. [31]	$-\left(\frac{dP}{dz}\right)_F = \frac{2f_{tp}v_f G^2}{D_h} \left(1 + x \frac{v_{fg}}{v_f}\right)$ $f_{tp} = 16\text{Re}_{tp}^{-1} \text{ for } \text{Re}_{tp} < 2000$ $f_{tp} = 0.079\text{Re}_{tp}^{-0.25} \text{ for } 2000 \leq \text{Re}_{tp} < 20,000$ $f_{tp} = 0.046\text{Re}_{tp}^{-0.2} \text{ for } \text{Re}_{tp} \geq 20,000$ $\text{Re}_{tp} = \frac{GD_h}{\mu_{tp}}$ $\frac{1}{\mu_{tp}} = \frac{x}{\mu_g} + \frac{1-x}{\mu_f}$	Homogeneous Equilibrium Model
Lockhart and Martinelli [32]	$\left(\frac{dP}{dz}\right)_F = \left(\frac{dP}{dz}\right)_f \phi_f^2, \phi_f^2 = 1 + \frac{C}{X} + \frac{1}{X^2}, X^2 = \frac{(dP/dz)_f}{(dP/dz)_g}$ $C_{vv} = 5, C_{tv} = 10, C_{vt} = 12, C_{tt} = 20$	$D_h = 1.49\text{--}25.83$ mm, adiabatic
Akers et al. [33]	$-\left(\frac{dP}{dz}\right)_F = \frac{2f_{tp}v_f G^2}{D_h} \left(1 + x \frac{v_{fg}}{v_f}\right)$ $f_{tp} = 16\text{Re}_{tp}^{-1} \text{ for } \text{Re}_{tp} < 2000$ $f_{tp} = 0.079\text{Re}_{tp}^{-0.25} \text{ for } 2000 \leq \text{Re}_{tp} < 20,000$ $f_{tp} = 0.046\text{Re}_{tp}^{-0.2} \text{ for } \text{Re}_{tp} \geq 20,000$ $\text{Re}_{tp} = \frac{GD_h}{\mu_{tp}}$ $\mu_{tp} = \frac{\mu_f}{\left[(1-x) + x \left(\frac{\mu_g}{\mu_f}\right)^{0.5}\right]}$	Homogeneous Equilibrium Model
Beattie and Whalley [34]	$-\left(\frac{dP}{dz}\right)_F = \frac{2f_{tp}v_f G^2}{D_h} \left(1 + x \frac{v_{fg}}{v_f}\right)$ $f_{tp} = 16\text{Re}_{tp}^{-1} \text{ for } \text{Re}_{tp} < 2000$ $f_{tp} = 0.079\text{Re}_{tp}^{-0.25} \text{ for } 2000 \leq \text{Re}_{tp} < 20,000$ $f_{tp} = 0.046\text{Re}_{tp}^{-0.2} \text{ for } \text{Re}_{tp} \geq 20,000$ $\text{Re}_{tp} = \frac{GD_h}{\mu_{tp}}$ $\mu_{tp} = \omega \mu_g + (1 - \omega)(1 + 2.5\omega)\mu_f$ $\omega = \frac{xv_{fg}}{v_f + xv_{fg}}$	Homogeneous Equilibrium Model
Müller-Steinhagen and Heck [35]	$\left(\frac{dP}{dz}\right)_F = \left\{ \left(\frac{dP}{dz}\right)_{fo} + 2 \left[ \left(\frac{dP}{dz}\right)_{go} - \left(\frac{dP}{dz}\right)_{fo} \right] x \right\} (1-x)^{1/3} + \left(\frac{dP}{dz}\right)_{go} x^3$	$D = 4\text{--}392$ mm, air–water, water, hydrocarbons, refrigerants
Jung and Radermacher [36]	$\left(\frac{dP}{dz}\right)_F = \left(\frac{dP}{dz}\right)_{fo} \phi_{fo}^2, \phi_{fo}^2 = 12.82X_{tt}^{1.47} (1-x)^{1.8},$ $X_{tt} = \left(\frac{\mu_f}{\mu_g}\right)^{0.1} \left(\frac{1-x}{x}\right)^{0.9} \left(\frac{\rho_g}{\rho_f}\right)^{0.5}$	$D = 9.1$ mm, annular flow boiling, pure and mixed refrigerants
Mishima and Hibiki [37]	$\left(\frac{dP}{dz}\right)_F = \left(\frac{dP}{dz}\right)_f \phi_f^2, \phi_f^2 = 1 + \frac{C}{X} + \frac{1}{X^2}$ <p>For rectangular channel, <math>C = 21[1 - \exp(-0.319D_h)]</math>; <math>D_h</math> [mm] For circular tube, <math>C = 21[1 - \exp(-0.333D)]</math>; <math>D</math> [mm]</p>	$D = 1.05\text{--}4.08$ mm, adiabatic, air–water
Yang and Webb [38]	$\left(\frac{dP}{dz}\right)_F = -0.87\text{Re}_{eq}^{0.12} f_{fo} \frac{G_{eq}^2 v_f}{D_h}, \text{Re}_{eq} = \frac{G_{eq} D_h}{\mu_f}, G_{eq} = G \left[ (1-x) + x \left(\frac{\rho_f}{\rho_g}\right)^{0.5} \right]$	$D = 1.56, 2.64$ mm, adiabatic, R12, $\text{Re}_{fo} > 2500$
Wang et al. [39]	<p>For <math>G \geq 200</math> kg/m<sup>2</sup> s,  <math display="block">\left(\frac{dP}{dz}\right)_F = \left(\frac{dP}{dz}\right)_g \phi_g^2, \phi_g^2 = 1 + 9.4X^{0.62} + 0.564X^{2.45}</math></p> <p>For <math>G &lt; 200</math> kg/m<sup>2</sup> s,  <math display="block">\left(\frac{dP}{dz}\right)_F = \left(\frac{dP}{dz}\right)_f \phi_f^2, \phi_f^2 = 1 + \frac{C}{X} + \frac{1}{X^2},</math> <math display="block">C = 4.566 \times 10^{-6} X^{0.128} \text{Re}_{fo}^{0.938} \left(\frac{v_f}{v_g}\right)^{2.15} \left(\frac{\mu_f}{\mu_g}\right)^{5.1}</math></p>	$D = 6.5$ mm, adiabatic, R22, R134a, R407C
Yan and Lin [40]	$\left(\frac{dP}{dz}\right)_F = -0.22\text{Re}_{eq}^{-0.1} \frac{G^2}{D_h} [v_f + x v_{fg}]$	$D = 2.0$ mm, boiling, R134a
Tran et al. [41]	$\left(\frac{dP}{dz}\right)_F = \left(\frac{dP}{dz}\right)_{fo} \phi_{fo}^2, N_{conf} = \sqrt{\frac{\sigma}{g(\rho_f - \rho_g) D_h}} \left( = \sqrt{\frac{1}{Bd}} \right)$ $\phi_{fo}^2 = 1 + \left[ 4.3 \frac{(dP/dz)_{go}}{(dP/dz)_{fo}} - 1 \right] \left[ N_{conf} x^{0.875} (1-x)^{0.875} + x^{1.75} \right]$	$D_h = 2.40\text{--}2.92$ mm, boiling, refrigerants
Yu et al. [42]	$\left(\frac{dP}{dz}\right)_F = \left(\frac{dP}{dz}\right)_f \phi_f^2, \phi_f^2 = \left[ 18.65 \left(\frac{v_f}{v_g}\right)^{0.5} \left(\frac{1-x}{x}\right) \frac{\text{Re}_{fo}^{0.1}}{\text{Re}_f^{0.25}} \right]^{-1.9}$	$D = 2.98$ mm, boiling, water
Sun and Mishima [43]	$\left(\frac{dP}{dz}\right)_F = \left(\frac{dP}{dz}\right)_f \phi_f^2, \phi_f^2 = 1 + \frac{C}{X} + \frac{1}{X^2}$ <p>For <math>\text{Re}_f &lt; 2000</math> and <math>\text{Re}_g &lt; 2000</math>,  <math display="block">C = 26 \left( 1 + \frac{\text{Re}_f}{1000} \right) \left\{ 1 - \exp\left(\frac{-0.153}{0.27N_{conf} + 0.8}\right) \right\}</math></p> <p>For <math>\text{Re}_f \geq 2000</math> and <math>\text{Re}_g \geq 2000</math>,  <math display="block">C = 1.79 \left(\frac{\text{Re}_g}{\text{Re}_f}\right)^{0.4} \left(\frac{1-x}{x}\right)^{0.5}</math></p>	$D_h = 0.506\text{--}12$ mm, air–water, refrigerants, CO <sub>2</sub>
Li and Wu [44]	$\left(\frac{dP}{dz}\right)_F = \left(\frac{dP}{dz}\right)_f \phi_f^2, \phi_f^2 = 1 + \frac{C}{X} + \frac{1}{X^2}, Bd = \frac{g(\rho_f - \rho_g) D_h^2}{\sigma}$ <p>For <math>Bd \leq 1.5</math>, <math>C = 11.9Bd^{0.45}</math>  For <math>1.5 &lt; Bd \leq 11</math>, <math>C = 109.4(Bd\text{Re}_f^{0.5})^{-0.56}</math>  For <math>Bd &gt; 11</math>, Beattie and Whalley [34] correlation is recommended</p>	$D_h = 0.148\text{--}3.25$ mm, adiabatic, refrigerants, ammonia, propane, nitrogen
Li and Wu [45]	<p>For <math>Bd &lt; 0.1</math>,  <math display="block">\left(\frac{dP}{dz}\right)_F = \left(\frac{dP}{dz}\right)_f \phi_f^2, \phi_f^2 = 1 + \frac{C}{X} + \frac{1}{X^2}, C = 5.60Bd^{0.28}</math></p> <p>For <math>Bd \geq 0.1</math> and <math>Bd\text{Re}_f^{0.5} \leq 200</math>,  <math display="block">\left(\frac{dP}{dz}\right)_F = \left(\frac{dP}{dz}\right)_{fo} \phi_{fo}^2, \phi_{fo}^2 = (1-x)^2 + 2.87x^2 P_R^{-1} + 1.54Bd^{0.19} \left(\frac{\rho_f - \rho_g}{\rho_f}\right)^{0.81}</math></p> <p>For <math>Bd\text{Re}_f^{0.5} &gt; 200</math>, Beattie and Whalley [34] correlation is recommended</p>	$D_h = 0.148\text{--}3.25$ mm, adiabatic, refrigerants, ammonia, propane, nitrogen

Table 2 (continued)

Author(s)	Equation(s)	Remarks
Kim and Mudawar [46]	$\left(\frac{dP}{dz}\right)_F = \left(\frac{dP}{dz}\right)_f \phi_f^2$ <p>where <math>\phi_f^2 = 1 + \frac{C}{X} + \frac{1}{X^2}</math>, <math>X^2 = \frac{(dP/dz)_f}{(dP/dz)_g}</math></p> $-\left(\frac{dP}{dz}\right)_f = \frac{2f_f \nu_f G^2 (1-x)^2}{D_h}, \quad -\left(\frac{dP}{dz}\right)_g = \frac{2f_g \nu_g G^2 x^2}{D_h}$ $f_k = 16 \text{Re}_k^{-1} \text{ for } \text{Re}_k < 2000$ $f_k = 0.079 \text{Re}_k^{-0.25} \text{ for } 2000 \leq \text{Re}_k < 20,000$ $f_k = 0.046 \text{Re}_k^{-0.2} \text{ for } \text{Re}_k \geq 20,000$ <p>for laminar flow in rectangular channel,</p> $f_k \text{Re}_k = 24(1 - 1.3553\beta + 1.9467\beta^2 - 1.7012\beta^3 + 0.9564\beta^4 - 0.2537\beta^5)$ <p>where subscript <math>k</math> denotes <math>f</math> or <math>g</math> for liquid and vapor phases, respectively,</p> $\text{Re}_f = \frac{G(1-x)D_h}{\mu_f}, \text{Re}_g = \frac{GxD_h}{\mu_g}, \text{Re}_{fo} = \frac{GD_h}{\mu_f}, \text{Su}_{go} = \frac{\rho_g \sigma D_h}{\mu_g^2}$ $\text{We}_{fo} = \frac{G^2 D_h}{\rho_f \sigma}, \text{Bo} = \frac{q_w''}{Ch_{fg}}$ <p><math>C_{non-boiling}</math> (for adiabatic cases):</p> $\text{Re}_f \geq 2000, \text{Re}_g \geq 2000 \text{ (tt): } 0.39 \text{Re}_{fo}^{0.03} \text{Su}_{go}^{0.10} \left(\frac{\rho_f}{\rho_g}\right)^{0.35}$ $\text{Re}_f \geq 2000, \text{Re}_g < 2000 \text{ (tv): } 8.7 \times 10^{-4} \text{Re}_{fo}^{0.17} \text{Su}_{go}^{0.50} \left(\frac{\rho_f}{\rho_g}\right)^{0.14}$ $\text{Re}_f < 2000, \text{Re}_g \geq 2000 \text{ (vt): } 0.0015 \text{Re}_{fo}^{0.59} \text{Su}_{go}^{0.19} \left(\frac{\rho_f}{\rho_g}\right)^{0.36}$ $\text{Re}_f < 2000, \text{Re}_g < 2000 \text{ (vv): } 3.5 \times 10^{-5} \text{Re}_{fo}^{0.44} \text{Su}_{go}^{0.50} \left(\frac{\rho_f}{\rho_g}\right)^{0.48}$ <p><math>C</math> (for cases with heat transfer):</p> $\text{Re}_f \geq 2000: C_{non-boiling} \left[ 1 + 60 \text{We}_{fo}^{0.32} \left(\text{Bo} \frac{\rho_u}{\rho_f}\right)^{0.78} \right]$ $\text{Re}_f < 2000: C_{non-boiling} \left[ 1 + 530 \text{We}_{fo}^{0.52} \left(\text{Bo} \frac{\rho_u}{\rho_f}\right)^{1.09} \right]$	Details of parametric range in [46]

point calculated by interpolating between experimental inlet and exit qualities.

correlation's ability to capture the trends described in the preceding sections.

5.3. Assessment of accuracies of models and correlations

Tables 3–5 show MAE values of pressure drop models and correlations for vertical upflow, vertical downflow, and horizontal flow, respectively. Each orientation subset of the overall database is further subdivided into single-sided and double-sided heating, low and high inlet quality (with  $x_{e,in} = 0.20$  used as transition point), and low and high flow velocity (with  $G = 1200 \text{ kg/m}^2 \text{ s}$  used as transition value). These divisions are intended to assess each

5.3.1. Vertical upflow predictions

Analyzing the results for vertical upflow presented in Table 3, the correlations by Kim and Mudawar [46] and Sun and Mishima [43] are seen to provide the best results, evidenced by overall MAE values of 26.8% and 28.8%, respectively. The mixture viscosity models by McAdams et al. [31], Akers et al. [33], and Beattie and Whalley [34], which all rely upon the Homogeneous Equilibrium Model (HEM), also perform reasonably well, yielding MAE values of 47.1%, 51.5%, and 52.5%, respectively. Correlations by Mishima

Table 3 Mean absolute error of pressure drop correlations evaluated using vertical upflow data.

Model/correlation	Vertical upflow						
	Total (214 data points) (%)	Single-sided (105 data points) (%)	Double-sided (109 data points) (%)	$x_{e,in} < 0.2$ (155 data points) (%)	$x_{e,in} \geq 0.2$ (59 data points) (%)	$G < 1200 \text{ kg/m}^2 \text{ s}$ (159 data points) (%)	$G \geq 1200 \text{ kg/m}^2 \text{ s}$ (55 data points) (%)
McAdams et al. [31]	52.5	57.0	48.1	51.0	56.3	49.8	60.2
Lockhart and Martinelli [32]	77.5	89.0	66.5	89.4	46.3	76.1	81.6
Akers et al. [33]	47.1	51.7	42.7	46.6	48.3	43.5	57.6
Beattie and Whalley [34]	51.5	55.9	47.2	49.9	55.7	48.9	58.9
Müller-Steinhagen and Heck [35]	72.6	74.9	70.5	72.3	73.6	69.3	82.2
Jung and Radermacher [36]	70.7	73.1	68.4	71.5	68.7	66.8	82.1
Mishima and Hibiki [37]	40.9	48.5	33.6	46.8	25.3	43.0	34.9
Yang and Webb [38]	58.9	61.2	56.7	64.0	45.6	53.8	73.8
Wang et al. [39]	49.3	56.8	42.1	50.4	46.5	52.9	38.8
Yan and Lin [40]	99.3	104.6	94.2	78.8	153.1	112.9	60.1
Tran et al. [41]	57.4	73.0	42.5	73.7	14.6	47.7	85.5
Yu et al. [42]	70.8	73.2	68.5	71.6	68.8	67.7	79.8
Sun and Mishima [43]	28.8	34.7	23.1	32.4	19.2	31.8	20.1
Li and Wu [44]	51.5	55.9	47.2	49.9	55.7	48.9	58.9
Li and Wu [45]	51.5	55.9	47.2	49.9	55.7	48.9	58.9
Kim and Mudawar [46]	26.8	32.5	21.3	30.1	17.9	20.7	44.3

**Table 4**  
Mean absolute error of pressure drop correlations evaluated using vertical downflow data.

Model/correlation	Vertical downflow						
	Total (218 data points) (%)	Single-sided (101 data points) (%)	Double-sided (117 data points) (%)	$x_{e,in} < 0.2$ (151 data points) (%)	$x_{e,in} \geq 0.2$ (67 data points) (%)	$G < 1200$ kg/m <sup>2</sup> s (158 data points) (%)	$G \geq 1200$ kg/m <sup>2</sup> s (60 data points) (%)
McAdams et al. [31]	58.3	62.9	54.4	57.6	60.1	57.4	60.9
Lockhart and Martinelli [32]	84.1	94.8	74.8	100.0	48.2	79.3	96.6
Akers et al. [33]	52.7	56.8	49.2	52.9	52.2	50.8	57.8
Beattie and Whalley [34]	57.3	61.8	53.4	56.3	59.5	56.5	59.4
Müller-Steinhagen and Heck [35]	90.6	94.1	87.6	94.8	81.2	90.5	91.0
Jung and Radermacher [36]	88.5	91.9	85.5	93.9	76.3	87.6	90.9
Mishima and Hibiki [37]	44.6	51.1	39.0	52.1	27.6	45.8	41.4
Yang and Webb [38]	75.9	78.7	73.5	85.8	53.7	73.7	81.7
Wang et al. [39]	50.3	57.7	43.9	54.0	42.0	54.3	39.7
Yan and Lin [40]	99.3	108.9	91.0	81.2	140.2	113.0	63.1
Tran et al. [41]	63.8	72.9	56.0	83.2	20.2	49.9	100.5
Yu et al. [42]	88.6	92.2	85.5	93.9	76.7	88.7	88.3
Sun and Mishima [43]	31.1	36.3	26.7	34.5	23.6	36.0	18.4
Li and Wu [44]	57.3	61.8	53.4	56.3	59.5	56.5	59.4
Li and Wu [45]	57.3	61.8	53.4	56.3	59.5	56.5	59.4
Kim and Mudawar [46]	42.3	47.9	37.5	50.1	24.8	40.0	48.4

**Table 5**  
Mean absolute error of pressure drop correlations evaluated using horizontal flow data.

Model/correlation	Horizontal flow							
	Total (397 data points) (%)	Top heated (129 data points) (%)	Bottom heated (128 data points) (%)	Double-sided (140 data points) (%)	$x_{e,in} < 0.2$ (281 data points) (%)	$x_{e,in} \geq 0.2$ (116 data points) (%)	$G < 1200$ kg/m <sup>2</sup> s (279 data points) (%)	$G \geq 1200$ kg/m <sup>2</sup> s (118 data points) (%)
McAdams et al. [31]	54.6	52.7	60.5	51.0	59.6	42.6	50.8	63.7
Lockhart and Martinelli [32]	148.1	152.7	160.5	132.6	174.0	85.4	177.2	79.3
Akers et al. [33]	52.6	50.3	59.0	49.0	59.9	35.0	49.1	61.0
Beattie and Whalley [34]	54.0	51.7	60.1	50.6	59.0	42.0	50.5	62.3
Müller-Steinhagen and Heck [35]	74.1	79.1	73.6	69.9	75.7	70.0	68.2	87.9
Jung and Radermacher [36]	71.4	76.1	71.4	67.2	74.9	63.0	64.4	88.1
Mishima and Hibiki [37]	96.3	93.7	111.9	84.5	111.3	60.2	123.3	32.6
Yang and Webb [38]	59.5	63.5	60.5	54.8	67.8	39.3	51.0	79.5
Wang et al. [39]	110.6	109.4	123.7	99.7	119.0	90.1	142.3	35.7
Yan and Lin [40]	188.4	182.1	202.8	181.1	168.3	237.3	245.0	54.6
Tran et al. [41]	129.1	140.2	148.7	101.0	163.2	46.6	141.3	100.3
Yu et al. [42]	72.9	78.4	72.2	68.6	75.6	66.5	67.4	86.0
Sun and Mishima [43]	73.6	71.5	86.2	64.1	84.3	47.9	97.5	17.3
Li and Wu [44]	54.0	51.7	60.1	50.6	59.0	42.0	50.5	62.3
Li and Wu [45]	54.0	51.7	60.1	50.6	59.0	42.0	50.5	62.3
Kim and Mudawar [46]	50.8	49.5	55.5	47.9	56.1	38.2	50.0	52.9

and Hibiki [37] and Yang and Webb [38] perform similarly, with MAE values of 40.9% and 49.3%, respectively.

Immediately noticeable within the table are the identical performances of both correlations by Li and Wu [44,45] and Beattie and Whalley [34]. This is due to the formulation of both correlations by Li and Wu, which require that for  $BdRe_f^{0.5} > 200$ , where  $Bd$  is the Bond number and  $Re_f$  the liquid Reynolds number, the correlation by Beattie and Whalley should be used. For the present database, this condition is satisfied for all data points, explaining the duplicate values of MAE for these three correlations.

For all models/correlations evaluated, better results are achieved for double-sided heating compared to single-sided, with MAE decreasing by up to 22.5%. This can be explained by the fact that the majority of pressure drop correlations were developed for uniform circumferential heating. Analysis of results for the two quality ranges evaluated reveals no clear trends. Some correlations, such as Yan and Lin's [40], exhibit a significant decrease in predictive accuracy for higher qualities. Other correlations, such as those of Lockhart and Martinelli [32] and Tran et al. [41],

perform better at higher qualities. In the case of Tran et al., MAE decreases from 73.7% for  $x_{e,in} < 0.20$  to 14.6% for  $x_{e,in} \geq 0.20$ . Finally, trends for low versus high mass velocities are similarly mixed, with inconsistent behavior across all correlations.

### 5.3.2. Vertical downflow predictions

Similar to vertical upflow, Table 4 reveals that correlations by Kim and Mudawar [46] and Sun and Mishima [43] provide the best predictions for vertical downflow, with MAE of 42.3% and 31.1%, respectively. Overall, MAE is higher for all correlations in vertical downflow compared to vertical upflow, with the exception of Yan and Lin's [40], whose MAE decreases by 1.0%. The inferior predictions for vertical downflow can be ascribed to the secondary role of body force driving vapor motion against that of liquid, as previously discussed in conjunction with Fig. 6(b).

Just as in vertical upflow, all correlations perform better for cases of double-sided heating compared to their single-sided counterparts. Here, however, results generally improve for higher qualities, with the exceptions of Beattie and Whalley [34] (and, by

extension, Li and Wu [44,45]), McAdams et al. [31], and Yan and Lin [40]. The correlation by Tran et al. [41] again exhibits marked improvement for higher qualities, with MAE decreasing from 83.2% for  $x_{e,in} < 0.20$  to 20.2% for  $x_{e,in} \geq 0.20$ .

Results for low versus high mass velocities are again mixed, with some correlations showing improvement while others performing worse.

5.3.3. Horizontal flow predictions

MAE values for horizontal flow in Table 5 indicate that, while the nearly unilateral increase in MAE as seen for vertical downflow is not present, many correlations show drastic increases in MAE. Those by Lockhart and Martinelli [32], Mishima and Hibiki [37], Wang et al. [39], Yan and Lin [40], Tran et al. [41], and Sun and Mishima [43] all show significant increases in MAE compared to vertical upflow and vertical downflow. No single correlation does well at predicting pressure drop for horizontal flow, with the lowest MAE of 50.8% narrowly belonging to Kim and Mudawar [46].

The general trend of decreased MAE for double-sided heating is again present for the majority of correlations, and similar to vertical downflow, all but Yan and Lin's [40] exhibit better performance for higher quality ranges. Results for the different mass velocity ranges examined are again mixed.

5.4. Statistical spread in predictions of models/correlations

Fig. 11(a)–(c) compare experimental pressure drop,  $\Delta P_{tp,exp}$ , to predicted pressure drop,  $\Delta P_{tp,pred}$ , using HEM with three different two-phase viscosity relations. Shown in each are values of overall MAE along with  $\theta$  and  $\zeta$ , which indicate the percentage of predictions falling within 30% and 50% of experimental values, respectively. Interestingly, this relatively simple model provides fair predictions of the data, evidenced by MAE values of 55.0%, 51.2%, and 54.2% using the viscosity relations of McAdams et al. [31], Akers et al. [33], and Beattie and Whalley [34], respectively. However, there is appreciable spread around the mean, indicated by low values of both  $\theta$  and  $\zeta$ , especially for low values of pressure drop.

Fig. 12(a)–(k) show similar plots comparing  $\Delta P_{tp,exp}$  to predictions of 11 different empirical correlations. Excluded here are comparisons based on the correlations by Li and Wu [44,45] since, as discussed earlier, these correlations yield predictions identical to those of Beattie and Whalley [34], Fig. 11(c), for the operating conditions of the present study. Overall, the correlations of Kim and Mudawar [46] and Sun and Mishima [43] offer the best predictive capability, evidenced by total MAE values of 42.4% and 50.9%, respectively.

Virtually all empirical correlations display appreciable spread in pressure drop predictions. This can be attributed to two causes: (1) over-prediction of pressure drop for many horizontal flow cases, especially at low mass velocities where the vapor stratification phenomenon described in Fig. 7(a) and (b) is prevalent, and (2) under-prediction of pressure drop for many low mass velocity vertical downflow cases, where the secondary effect of body force attempting to drive vapor counter to the flow direction is not accounted for.

These two effects lead to the ‘fish-tail’ shapes on the low end of most plots in Fig. 12. For moderate values of pressure drop, most correlations perform reasonably well, managing to keep at least a portion of predictions within the  $\pm 30\%$  bounds. As pressure drop increases, however, the majority of correlations struggle to accurately capture experimental trends, with only the correlation by Kim and Mudawar [46] exhibiting consistent success in the upper range. Overall, there is nearly an even split between correlations over-predicting and under-predicting pressure drop in the upper range, with six overshooting experimental values and seven (not

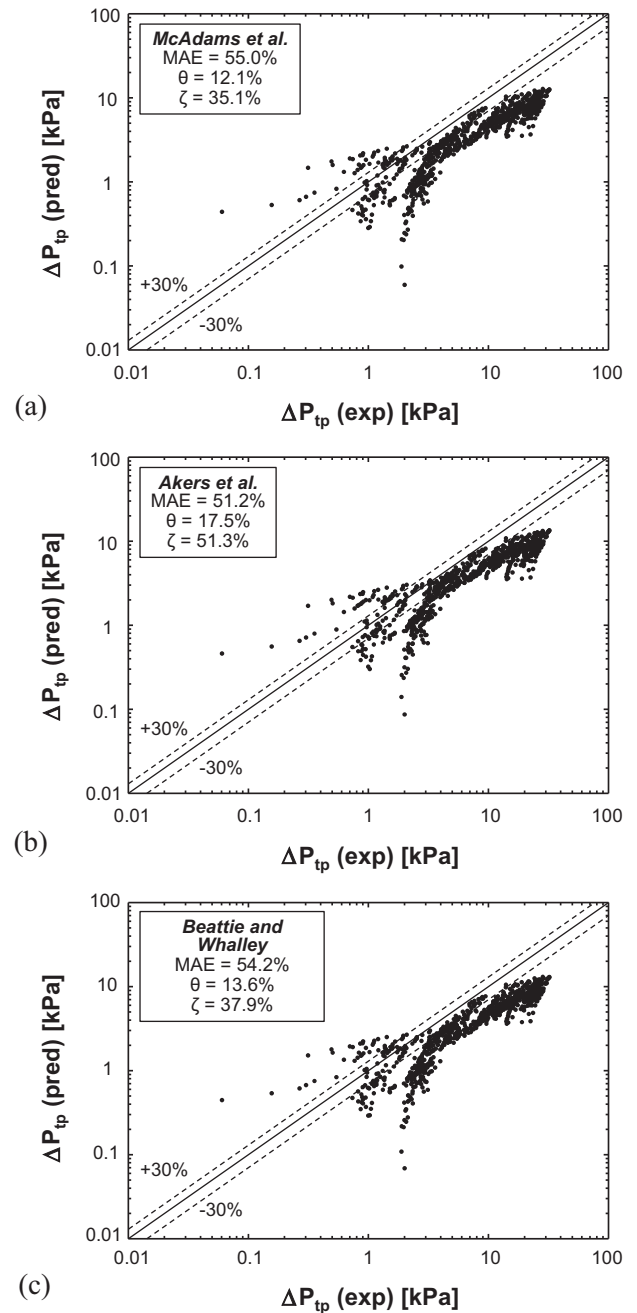
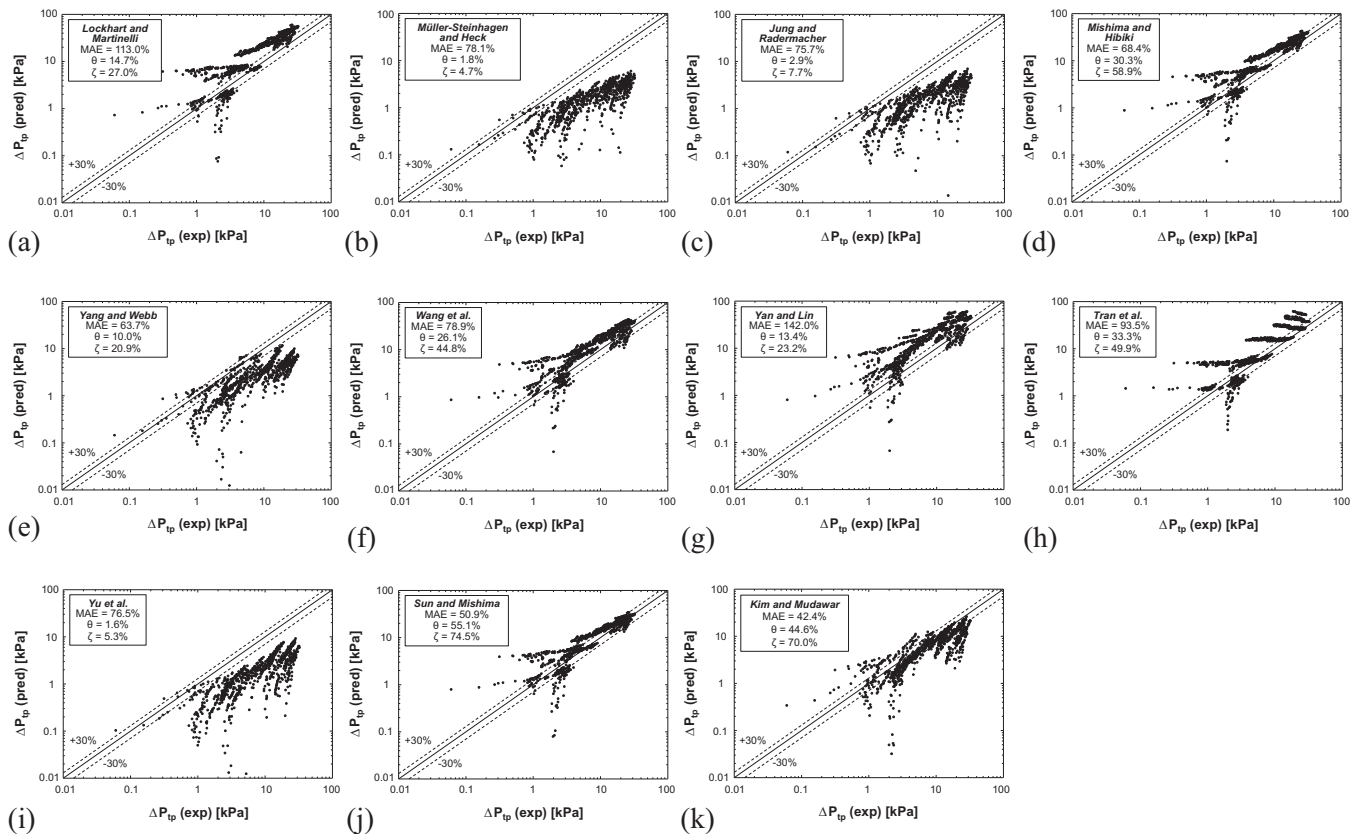


Fig. 11. Comparison of experimental pressure drop with predictions of Homogeneous Equilibrium Model (HEM) based on viscosity models of (a) McAdams et al. [31], (b) Akers et al. [33], and (c) Beattie and Whalley [34].

counting Li and Wu [44,45]) falling short. The superior performance of the Kim and Mudawar correlation can be traced to its ‘universal’ formulation. This correlation is based on a database composed of 2378 data points amassed from 16 sources. The database includes 9 working fluids, hydraulic diameters from 0.349 to 5.35 mm, mass velocities from 33 to 2,738 kg/m<sup>2</sup>s, qualities from 0 to 1, reduced pressures from 0.005 to 0.78, and both single-channel and multi-channel data.

No correlations evaluated here completely failed to capture experimental trends, but overall results are hampered by inconsistency across the full range of operating conditions. Secondary body force effects described earlier for horizontal flow and vertical downflow are missed by the majority of correlations, and slight offsets in trend degrade accuracy at high pressure drops.



**Fig. 12.** Comparison of experimental pressure drop with predictions of correlations of (a) Lockhart and Martinelli [32], (b) Müller-Steinhagen and Heck [35], (c) Jung and Radermacher [36], (d) Mishima and Hibiki [37], (e) Yang and Webb [38], (f) Wang et al. [39], (g) Yan and Lin [40], (h) Tran et al. [41], (i) Yu et al. [42], (j) Sun and Mishima [43], and (k) Kim and Mudawar [46].

## 6. Conclusions

This study examined two-phase pressure drop associated with flow boiling of FC-72 in a rectangular channel subjected to single-sided and double-sided heating. Orientations of vertical upflow, vertical downflow, and horizontal flow were tested over broad ranges of positive inlet quality and mass velocity. Both transient and time-averaged experimental results for two-phase pressure drop were presented, and parametric trends evaluated to better understand the complex interactions between flow inertia and body force. Commonly used predictive correlations for pressure drop were also presented and evaluated using 829 pressure drop data points. Key findings from this study are as follows:

- (1) Analysis of temporal pressure records reveals the dominant frequency of oscillation for all orientations is in the range of 0.3–3 Hz, behavior characteristic of “density wave oscillations”. Secondary oscillations are also prevalent at higher frequencies for vertical upflow and vertical downflow, along with pump-induced sharp peaks at 20, 40, 60, and 80 Hz.
- (2) The amplitude of pressure drop oscillations is highest for vertical upflow followed, in order, by vertical downflow and horizontal flow. Increases in mass velocity and heat flux increase the amplitude (and in some cases, frequency) of oscillations for all cases, while the effect of increasing inlet quality is inconsistent across orientations.
- (3) Time-averaged pressure drop results for the different orientations demonstrate similar trends at high mass velocities, while low mass velocities exhibit significant deviations due to appreciable differences in body force effects. Increases in inlet quality and/or heat flux increase pressure drop due to increased flow acceleration.

- (4) Correlations for pressure drop predict data with varying degrees of success, with the majority capable of correctly capturing overall trends in experimental data. However, secondary effects of body force prevalent at low mass velocities are missed. They include decreased pressure drop in horizontal flow with single-sided heating due to vapor blanketing, and increased pressure drop in vertical downflow due to buoyancy tending to drive vapor opposite the flow direction.

## Acknowledgements

The authors are grateful for the financial support provided by the National Aeronautics and Space Administration (NASA) under Grant No. NNX13AB01G, and technical support of the NASA Glenn Research Center, Cleveland, Ohio. This work was also supported by NASA Space Technology Research Fellowship Grant No. NNX15AP29H.

## References

- [1] I. Mudawar, Two-phase micro-channel heat sinks: theory, applications and limitations, *J. Electron. Packag.* – *Trans. ASME* 133 (2011) 041002-2.
- [2] S. Lee, I. Mudawar, M.M. Hasan, Thermal analysis of hybrid single-phase, two-phase and heat pump thermal control system (TCS) for future spacecraft, *Appl. Therm. Eng.* 100 (2016) 190–214.
- [3] F.P. Chiramonte, J.A. Joshi, Workshop on critical issues in microgravity fluids, transport, and reaction processes in advanced human support technology – final report, NASA TM-2004-212940, 2004.
- [4] The National Academies, *Recapturing a Future for Space Exploration: Life and Physical Sciences Research for a New Era*, National Academies Press, Washington, DC, 2011.
- [5] P.J. Marto, V.J. Lepere, Pool boiling heat transfer from enhanced surfaces to dielectric fluids, *J. Heat Transfer Trans. ASME* 104 (1982) 292–299.

- [6] I. Mudawar, T.M. Anderson, Optimization of extended surfaces for high flux chip cooling by pool boiling, *J. Electron. Packag.* – *Trans. ASME* 115 (1993) 89–100.
- [7] J.A. Shmerler, I. Mudawar, Local heat transfer coefficient in wavy free-falling turbulent liquid films undergoing uniform sensible heating, *Int. J. Heat Mass Transfer* 31 (1988) 67–77.
- [8] J.A. Shmerler, I. Mudawar, Local evaporative heat transfer coefficient in turbulent free-falling liquid films, *Int. J. Heat Mass Transfer* 31 (1988) 731–742.
- [9] T.H. Lyu, I. Mudawar, Statistical investigation of the relationship between interfacial waviness and sensible heat transfer to a falling liquid film, *Int. J. Heat Mass Transfer* 34 (1991) 1451–1464.
- [10] K.E. Gungor, R.H.S. Winterton, General correlation for flow boiling in tubes and annuli, *Int. J. Heat Mass Transfer* 29 (1986) 351–358.
- [11] H.J. Lee, S.Y. Lee, Heat transfer correlation for boiling flows in small rectangular horizontal channels with low aspect ratios, *Int. J. Multiphase Flow* 27 (2001) 2043–2062.
- [12] S. Mukherjee, I. Mudawar, Smart pumpless loop for micro-channel electronic cooling using flat and enhanced surfaces, *IEEE Trans.-CPMT: Compon. Packag. Technol.* 26 (2003) 99–109.
- [13] M. Monde, T. Inoue, Critical heat flux in saturated forced convective boiling on a heated disk with multiple impinging jets, *J. Heat Transfer – Trans. ASME* 113 (1991) 722–727.
- [14] D.C. Wadsworth, I. Mudawar, Enhancement of single-phase heat transfer and critical heat flux from an ultra-high-flux simulated microelectronic heat source to a rectangular impinging jet of dielectric liquid, *J. Heat Transfer – Trans. ASME* 114 (1992) 764–768.
- [15] M.E. Johns, I. Mudawar, An ultra-high power two-phase jet-impingement avionic clamshell module, *J. Electron. Packag.* – *Trans. ASME* 118 (1996) 264–270.
- [16] D.D. Hall, I. Mudawar, Experimental and numerical study of quenching complex-shaped metallic alloys with multiple, overlapping sprays, *Int. J. Heat Mass Transfer* 38 (1995) 1201–1216.
- [17] L. Lin, R. Ponnappan, Heat transfer characteristics of spray cooling in a closed loop, *Int. J. Heat Mass Transfer* 46 (2003) 3737–3746.
- [18] I. Mudawar, D. Bharathan, K. Kelly, S. Narumanchi, Two-phase spray cooling of hybrid vehicle electronics, *IEEE Trans.-CPMT: Compon. Packag. Technol.* 32 (2009) 501–512.
- [19] M.K. Sung, I. Mudawar, Experimental and numerical investigation of single-phase heat transfer using a hybrid jet-impingement/micro-channel cooling scheme, *Int. J. Heat Mass Transfer* 49 (2006) 682–694.
- [20] S.M. Kim, I. Mudawar, Review of databases and predictive methods for pressure drop in adiabatic, condensing and boiling mini/micro-channel flow, *Int. J. Heat Mass Transfer* 77 (2014) 74–97.
- [21] N. Zuber, J.A. Findlay, Average volumetric concentration in two-phase flow systems, *J. Heat Transfer Trans. ASME* 87 (1965) 453–468.
- [22] J.A. Boure, A.E. Bergles, L.S. Tong, Review of two-phase flow instability, *Nucl. Eng. Des.* 25 (1973) 165–192.
- [23] L.C. Ruspini, C.P. Marcel, A. Clausse, Two-phase flow instabilities: a review, *Int. J. Heat Mass Transfer* 71 (2014) 521–548.
- [24] S. Kakac, B. Bon, A review of two-phase flow dynamic instabilities in tube boiling systems, *Int. J. Heat Mass Transfer* 51 (2008) 399–433.
- [25] L. Tadriss, Review on two-phase flow instabilities in narrow spaces, *Int. J. Heat Fluid Flow* 28 (2007) 54–62.
- [26] H. Zhang, I. Mudawar, M.M. Hasan, Experimental assessment of the effects of body force, surface tension force, and inertia on flow boiling CHF, *Int. J. Heat Mass Transfer* 45 (2002) 4079–4095.
- [27] H. Zhang, I. Mudawar, M.M. Hasan, Flow boiling CHF in microgravity, *Int. J. Heat Mass Transfer* 48 (2005) 3107–3118.
- [28] C.R. Kharangate, L.E. O'Neill, I. Mudawar, M.M. Hasan, H.K. Nahra, R. Balasubramaniam, N.R. Hall, A.M. Macner, J.R. Mackey, Effects of subcooling and two-phase inlet on flow boiling heat transfer and critical heat flux in a horizontal channel with one-sided and double-sided heating, *Int. J. Heat Mass Transfer* 91 (2015) 1187–1205.
- [29] C.R. Kharangate, L.E. O'Neill, I. Mudawar, M.M. Hasan, H.K. Nahra, R. Balasubramaniam, N.R. Hall, A.M. Macner, J.R. Mackey, Flow boiling and critical heat flux in horizontal channel with one-sided and double-sided heating, *Int. J. Heat Mass Transfer* 90 (2015) 323–338.
- [30] N.-C. Yen, Subharmonic Generation in Acoustic Systems, Technical Memorandum 65, Acoustics Research Laboratory, Harvard University, Cambridge, MA, 1971.
- [31] W.H. McAdams, W.K. Woods, L.C. Heroman, Vaporization inside horizontal tubes – II: benzene-oil mixture, *Trans. ASME* 64 (1942) 193–200.
- [32] R.W. Lockhart, R.C. Martinelli, Proposed correlation of data for isothermal two-phase, two-component flow in pipes, *Chem. Eng. Prog.* 45 (1949) 39–48.
- [33] W.W. Akers, H.A. Deans, O.K. Crosser, Condensing heat transfer within horizontal tubes, *Chem. Eng. Prog.* 54 (1958) 89–90.
- [34] D.R.H. Beattie, P.B. Whalley, A simple two-phase frictional pressure drop calculation method, *Int. J. Multiphase Flow* 8 (1982) 83–87.
- [35] H. Müller-Steinhagen, K. Heck, A simple friction pressure drop correlation for two-phase flow in pipes, *Chem. Eng. Process.* 20 (1986) 297–308.
- [36] D.S. Jung, R. Radermacher, Prediction of pressure drop during horizontal annular flow boiling of pure and mixed refrigerants, *Int. J. Heat Mass Transfer* 32 (1989) 2435–2446.
- [37] K. Mishima, T. Hibiki, Some characteristics of air-water two-phase flow in small diameter vertical tubes, *Int. J. Multiphase Flow* 22 (1996) 703–712.
- [38] C.Y. Yang, R.L. Webb, Friction pressure drop of R-12 in small hydraulic diameter extruded aluminum tubes with and without micro-fins, *Int. J. Heat Mass Transfer* 39 (1996) 801–809.
- [39] C.C. Wang, C.S. Chiang, D.C. Lu, Visual observation of two-phase flow pattern of R-22, R-134a, and R-407c in a 6.5-mm smooth tube, *Exp. Therm. Fluid Sci.* 15 (1997) 395–405.
- [40] Y.Y. Yan, T.F. Lin, Evaporation heat transfer and pressure drop of refrigerant R-134a in a small pipe, *Int. J. Heat Mass Transfer* 41 (1998) 4183–4194.
- [41] T.N. Tran, M.C. Chyu, M.W. Wambsganss, D.M. France, Two-phase pressure drop of refrigerants during flow boiling in small channels: experimental investigation and correlation development, *Int. J. Multiphase Flow* 26 (2000) 1739–1754.
- [42] W. Yu, D.M. France, M.W. Wambsganss, J.R. Hull, Two-phase pressure drop, boiling heat transfer, and critical heat flux to water in a small-diameter horizontal tube, *Int. J. Multiphase Flow* 28 (2002) 927–941.
- [43] L. Sun, K. Mishima, Evaluation analysis of prediction methods for two-phase flow pressure drop in mini-channels, *Int. J. Multiphase Flow* 35 (2009) 47–54.
- [44] W. Li, Z. Wu, A general correlation for adiabatic two-phase pressure drop in micro/mini-channels, *Int. J. Heat Mass Transfer* 53 (2010) 453–465.
- [45] W. Li, Z. Wu, Generalized adiabatic pressure drop correlations in evaporative micro/mini-channels, *Exp. Therm. Fluid Sci.* 35 (2011) 866–872.
- [46] S.-M. Kim, I. Mudawar, Universal approach to predicting two-phase frictional pressure drop for adiabatic and condensing mini/micro-channel flows, *Int. J. Heat Mass Transfer* 55 (2012) 3246–3261.
- [47] S.M. Zivi, Estimation of steady-state steam void-fraction by means of the principle of minimum entropy production, *J. Heat Transfer – Trans. ASME* 86 (1964) 247–252.